International Journal of Plasticity 145 (2021) 103073

Contents lists available at ScienceDirect

International Journal of Plasticity

journal homepage: www.elsevier.com/locate/ijplas

The predicted rate-dependent deformation behaviour and multistage strain hardening in a model heterostructured body-centered cubic high entropy alloy

Jing Peng[a,1], Li Li[a,1], Fang Li[a], Bin Liu[b], Sergey Zherebtsov[c], Qihong Fang[a,*], Jia Li[a,*], Nikita Stepanov[c], Yong Liu[b], Feng Liu[b,*], Peter K Liaw[d]

[a] *College of Mechanical and Vehicle Engineering, Hunan University, Changsha 410082, China*
[b] *State Key Laboratory of Powder Metallurgy, Central South University, Changsha 410083, China*
[c] *Laboratory of Bulk Nanostructured Materials, Belgorod State University, Belgorod 308015, Russia*
[d] *Department of Materials Science and Engineering, The University of Tennessee, Knoxville, TN 37996, United States*

ARTICLE INFO

Keywords:
High-entropy alloy
Multistage strengthening mechanism
Multiple phase transformation
Strain rate
Constitutive model

ABSTRACT

Heterostructured high-entropy alloys (HEAs) exhibit a good combination of strength and ductility. However, the deformation mechanisms and related mechanical properties of the heterogeneous nanostructured body-centred cubic (BCC) HEAs remain largely unrevealed. Here, we report the effect of the strain rate on the mechanical properties and microstructural evolution in the heterostructured $Al_3CoCrCuFeNi$ HEA with the gradient grain size ranging from 9 nm at the surface to 45 nm in the center using the large-scale atomic simulations. Based on the characterization of microstructure evolution from the atomic simulation, a microstructure-based constitutive model that utilizes a single parameter set is established to study the effects of the multiple strengthening mechanisms at various deformation stages on the strength and strain hardening of the heterostructured HEA under different strain rates. The results show that the plastic deformation mechanisms are strongly influenced by the strain rate in the range of 1×10^6 to 1×10^{10} s^{-1}. The dislocation and deformation twin are the main deformation mechanisms at the strain rate less than 1×10^8 s^{-1}. The deformation twinning cooperated with multiple phase transformations plays a pivotal role at the strain rate of 1×10^9 s^{-1}. The multiple phase transformations are the dominant plastic deformation model at the strain rate of 1×10^{10} s^{-1}, which is different from the classic plastic-deformation mode, including the dislocation and deformation twin in traditional alloys. This phenomenon is ascribed to various types of atomic interactions and atomic-size mismatches, which produce strong lattice distortion. In particular, a large number of edge dislocations are observed, which is extremely different from screw dislocations invariably generated in traditional BCC alloys, and thus, could be responsible for high strength. Furthermore, the stress-strain response of the $Al_3CoCrCuFeNi$ HEA is derived from the individual contributions of the lattice distortion, dislocation, grain boundary, deformation twin, phase transformation, and back-stress strengthening mechanisms. The heterogeneous grain boundaries and lattice distortion contribute the most to the yield strength, and the dislocation, deformation twin, phase transformation, and back stress dominate the strain hardening. Therefore, these

---

* Corresponding authors.
E-mail addresses: fangqh1327@hnu.edu.cn (Q. Fang), lijia123@hnu.edu.cn (J. Li), liufeng@csu.edu.cn (F. Liu).

[1] These authors contributed equally to this work.

https://doi.org/10.1016/j.ijplas.2021.103073
Received 25 April 2021; Received in revised form 12 July 2021;
Available online 17 July 2021

results highlight a new design strategy of HEAs to tailor their mechanical properties based on the partition of the multistage strengthening mechanisms by the heterostructure.

1. Introduction

Based on a progressive alloying design concept of the multiple principal elements, high-entropy alloys (HEAs) have been proposed (Yeh et al., 2004; Cantor et al., 2004; Shuang et al., 2020; Li et al., 2021; Wang et al., 2020), which greatly expanded the compositional space of metallic materials and showed a way of obtaining new alloys with performance superior to conventional materials. To meet constantly growing performance requirements in engineering applications, the ultra-high strength is often needed. One of the ways to achieve high strength is to refine grains to nanocrystalline level. However, due to the limited dislocation activity and strain hardening capacity in nanocrystalline metals, ductility is usually low (Chuvil'Deev et al., 2017). Therefore, the additional strengthening mechanisms must be activated to obtain the required strength-ductility combination. The development of heterogeneous structures can overcome this challenge due to the synergistic effect of regions with different structure parameters and mechanical behaviors (Zhu et al., 2021; Hasan et al., 2019). The heterostructure is usually a specially-designed heterogeneous certain microstructural component, such as the grains, twins, second phase particles, and precipitates (Wu et al., 2020; Li et al., 2018, 2020a). In the present work, the heterostructured body-centered-cubic (BCC) HEAs with gradient nanocrystalline structures are investigated.

Recently, some studies have found that if materials have both a heterogeneous structure and high density of grain boundaries, their strength and strain-hardening ability can be improved concurrently (Guo et al., 2019; Zhu et al., 2021). This trend is ascribed to the back-stress hardening mechanism derived from the heterogeneous grain structure to maintain the strain-hardening ability (Yang et al., 2018; Wang et al., 2020). Hence, the heterogeneous microstructure formation in HEAs can solve a conflict between the strength and ductility (Sathiyamoorthi and Kim, 2020). For example, heterogeneous lamellar structures in HEAs induce hetero-deformation and martensitic-strengthening mechanisms tofacilitate a balance between the strength and ductility (Zhang et al., 2020). A gradient hierarchical structure promoted nano-twinning and exceptional strain hardening capacity, and enhanced both strength and ductility of the $Al_{0.1}$CoCrFeNi HEAs (Chen et al., 2019). The multiple hardening mechanisms are activated in the eutectic HEA by the hetero-structure formation, intragranular composition modification, and ultra-fine grains, so that the prolonged stage of vivid strain hardening is displayed (Shi et al., 2020).

Furthermore, the origin of excellent mechanical properties of HEAs can be revealed effectively by investigating the plastic deformation mechanisms, such as dislocation glide, deformation twinning, and phase transformation. The corresponding mechanisms were systematically investigated, which depend on the chemistry and deformation conditions of the alloys (Bahramyan et al., 2020a; Hasan et al., 2019; Kireeva et al., 2020; Lam et al., 2020). For a group of HEAs with the same component and different Al concentrations, two completely different deformation mechanisms in $Al_{0.5}$CrCoFeCuNi and $Al_{1.5}$CrCoFeCuNi HEAs were revealed: the transformation-induced plasticity (TRIP) and twinning-induced plasticity (TWIP) (Bahramyan et al., 2020a). The deformation of the CoCrFeNiMn HEA with the gradient structure was controlled by the twin-twin and twin-dislocation interactions (Hasan et al., 2019). The analysis of the deformation behavior for the CoCrFeMnNi HEA also revealed that the deformation twinning is responsible for the strain hardening behavior and improves the strength and elongation simultaneously (Kireeva et al., 2020; Lam et al., 2020). However, the detailed understanding of deformation mechanisms and mechanical properties in heterogeneous BCC HEAs is still lacking, which limits their potential engineering applications.

To study the relationship between microstructures and mechanical properties intuitively, a molecular-dynamics (MD) method is a viable option that allows investigation of the idiographic deformation mechanisms from the atomic point of view. In our early atomic-simulation work, the formation and expansion of deformation twins in the AlCrFeCuNi HEA was revealed (Li et al., 2016); this phenomenon was further explored in the BCC HEA (Aitken et al., 2019). The mechanisms of the deformation-induced face-centered-cubic (FCC) to BCC transformation and bidirectional phase transformation between the FCC and the hexagonal close-packed (HCP) phases were elaborated in various HEAs (Li et al., 2018; Fang et al., 2019). Along with these works, a series of MD studies on phase transformation in TRIP-TWIP HEAs were reported (Bahramyan et al., 2020a). Recently, the phase transformations from crystallization to amorphization at the crack tip in the CoCrFeMnNi HEA were analyzed; the same processes were also verified by the thermodynamic theory (Li et al., 2020b). More recently, the indentation response, chemical short-range order, and radiation tolerance in HEAs were investigated by MD simulations (Cao et al., 2020; Jian et al., 2020; Lin et al., 2020; Zhao et al., 2021). Due to feasibility of MD stimulations for various phenomena listed above, in the current work the tensile deformation of a heterostructured BCC Al_3CoCrCuFeNi HEA is studied by the MD method.

Motivated by the intuitionistic comprehension of the deformation mechanism in the BCC HEA, using MD simulations, the quantitative physical basic model for the stress-strain response is essential. In the present work, the deformation mechanism and mechanical response of the gradient nano-grained (GNG) Al_3CoCrCuFeNi HEA during uniaxial tension with difference strain rates have been inspected through the MD simulations. The constitutive model considering the multistage strengthening mechanism is established by means of dynamic microstructures at the atomic level, which characterizes the relationship between the microstructures and mechanical properties in the gradient-nanocrystalline HEA.

2. Atomic-simulation method

The previous experiments (Sun et al., 2018; Sriharitha et al., 2014) show that the lattice parameter of the BCC Al_3CoCrCuFeNi HEA is 2.89 Å, and the atomic ratios of Al, Co, Cr, Cu, Fe, and Ni are 3:1:1:1:1:1. Based on these results, the atomic model of a gradient nanostructured BCC $Al_3CoCrCuFeNi$ HEA is built in Fig. 1a. The grain size of the $Al_3CoCrCuFeNi$ HEA increases gradually from 9.0 nm at the surface to 45.0 nm at the center, as shown in Fig. 1b. The $Al_3CoCrCuFeNi$ HEA sample has 190 grains with various orientations, which are constructed by the Voronoi method (Li et al., 2020c). For every grain, the z direction is set at the <110> direction, and other x and y directions are random. The $Al_3CoCrCuFeNi$ HEA sample contains 29,219,970 atoms and has the dimensions of $144 \times 200 \times 12.1\ nm^3$, where the thickness of the columnar grain is larger than the cutoff distance of 5 Å for meeting the periodicity along the z direction. Periodic boundary conditions are applying along x and z directions. The free boundary conditions are applying along the y directions, which leads to the free surface located in the small grain of the $Al_3CoCrCuFeNi$ HEA in Fig. 1b. To construct the desired $Al_3CoCrCuFeNi$ HEA sample, the atoms in the GNG Fe are randomly replaced by atoms of Al, Co, Cr, Cu, and Ni, as presented in Fig. 1a. Here, the gradient-nanostructured $Al_3CoCrCuFeNi$ HEA film of three-dimensional (3D) <110> textured (or columnar) grains is built. To highlight the gradient grain effect on the deformation response, the sample width (along the y-direction) is slightly larger than the sample length (along the x-direction), like the previous reports on the gradient nanostructured metals (Chen et al., 2019; Guo et al., 2019). Note that the common inhomogeneities in the HEAs, such as compositional variations, different types of defects, second phase particles, and precipitates, were not considered in the current work. Here, the grain-size change is considered as the only heterogeneity. The other heterogeneities will be considered in the future studies.

The velocities of all atoms are randomly set according to the Maxwell-Boltzmann distribution. Before the loading, the sample is first subjected to the energy minimization, using the conjugate gradient method and NVT dynamics (the canonical ensemble with a constant number of particles, volume, and temperature) at the temperature of 10 K for 100 picoseconds, to relax the system. Then, NPT dynamics (the isothermal-isobaric ensemble with a constant number of particles, pressure, and temperature) at the temperature of 10 K is performed for 100 picoseconds for further relaxation. A time step is 1 femtosecond. The uniaxial tensile loading with various rates from 1×10^6 to $1 \times 10^{10}\ s^{-1}$ is applied along the x direction under the NVT dynamics at the temperature of 10 K. The temperature in the NVT and NPT dynamics is adjusted by the Nose-Hoover method (Zepeda-Ruiz et al., 2017; Peng et al., 2021). The maximum engineering strain reaches 10%. An embedded-atom method potential (Daw et al., 1993; Zhou et al., 2004; Afkham et al., 2017; Li et al., 2019; Bahramyan et al., 2020b) is employed for the atom-atom interactions in the $Al_3CoCrCuFeNi$ HEA. However, it needs to be noted that the current interatomic potential cannot predict accurately the mechanical and physical properties of the Al-Co-Cr-Cu-Fe-Ni system HEAs, but it provides adequate tendencies of deformation behavior. Therefore, the high-quality six-element interatomic potential for the Al-Co-Cr-Cu-Fe-Ni system needs to be further developed, based on the results of experiments and first-principles calculations. In addition, the embedded atom method interatomic potentials have been applied to study the dislocation behavior and mechanical properties in the BCC HEAs (Rao et al., 2017; Li et al., 2019; Chen et al., 2020; Zhao et al., 2021). The MD simulations are computed by the open-source Large-scale Atomic/Molecular Massively Parallel Simulator code (Plimpton, 1995). The local atomic structure is analyzed by the common-neighbor analysis (CNA), and the microstructural evolution is presented via the Ovito software (Stukowski, 2009). Based on the value of CNA, the green color represents the FCC structure, the blue color stands for the BCC structure, and the white color means other structures, including the dislocation, grain boundary, and free surface in Fig. 1b.

The deformation mechanism of a nanocrystalline metal depends on the generalized planar fault energy (GPFE), which determines deformation twinning or dislocation glide. Figure 1c illustrates the curve of GPFE in the $Al_3CoCrCuFeNi$ HEA. γ_{us} is the unstable stacking fault energy, which represents the energy barrier for the a/6<111> dislocation to overcome the first layer stacking fault.

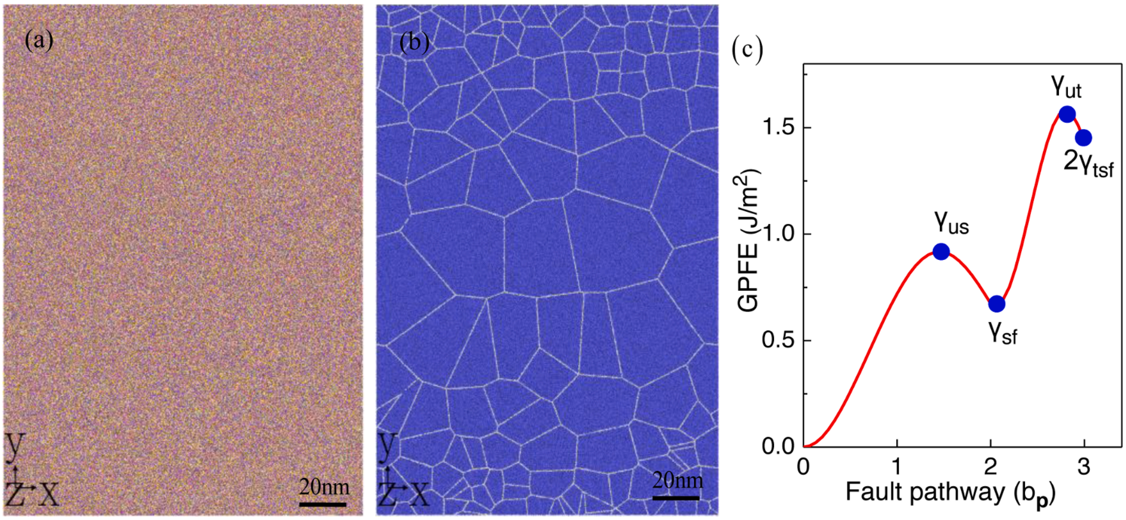

Fig. 1. The gradient nanostructured BCC $Al_3CoCrCuFeNi$ HEA. The atoms of the $Al_3CoCrCuFeNi$ HEA are colored based on the atomic type (a), where Al, Co, Cr, Cu, Fe, and Ni. The atoms are colored, based on the common-neighbor analysis (CNA) value (b), where represent the FCC structure, the HCP structure, the BCC structure, and other structure. The generalized planar fault energy (GPFE) curve on <111>{112} slip system of the heterostructured $Al_3CoCrCuFeNi$ HEA (c).

Similarly, γ_{sf} represents the stacking fault energy, γ_{ut} is the unstable twinning fault energy, and $2\gamma_{tsf}$ is the stable twin stacking fault energy. Here, the stacking fault energy and the stable twin stacking fault energy of the $Al_3CoCrCuFeNi$ HEA are 674 and 717 mJ/m^2, respectively. They are close to 637 and 710 mJ/m^2 in the BCC Fe (Ojha et al., 2014).

3. Results and discussion

The strain rate can strongly affect the mechanical properties and deformation mechanisms in the metals and alloys (Li et al., 2018; Zhu et al., 2012). Here, the $Al_3CoCrCuFeNi$ HEA is subject to plastic loading with different strain rates including 1×10^6, 1×10^7, 1×10^8, 1×10^9, and 1×10^{10} s^{-1}. The stress-strain curves of the heterostructured $Al_3CoCrCuFeNi$ HEA are clearly dependent on the strain rate (Fig. 2a). The obvious stress overshoot occurs at the strain rate less than 1×10^8 s^{-1}, which is relevant with the dominant mechanism of plastic deformation (Rida et al., 2020). For example, the dominant mode of plastic deformation in an $Al_{0.1}CrFeCoNi$ HEA at a high strain rate of 2.6×10^3 s^{-1} is twinning, leading to the significant work hardening (Kumar et al., 2015). The CoCrFeMnNi HEA exhibits the significant work-hardening behavior in the high strain-rate condition, which is easier to reach the critical twinning stress (Park et al., 2018; Nguyen et al., 2020). Thus, the flow stress increases with increasing the strain rate above 1×10^8 s^{-1}. The slope of the elastic region varies at the high strain rates of $\geq 1 \times 10^9$ s^{-1} because some plastic deformations may occur in the linear-elastic region at the extremely high strain rates (Wang et al., 2015). The previous work suggests that the relationship between the strain rate and yield strength complies with $\sigma = a + b\dot{\varepsilon}^c$ (Cowper et al., 1957; Li et al., 2020b,a), where σ is the yield strength, $\dot{\varepsilon}$ is the strain rate, and a,b, and c are the fitting parameters of the strain-rate sensitivity. Figure 2b reveals the change trend of the yield strength with the increasing strain rate. The corresponding fitting expression is $\sigma = 1.45 + 1.918 \times 10^{-4}\dot{\varepsilon}^{0.3851}$. Here, the stress first reaches a peak value, which is defined as the yield stress in Fig. 2b. For the no obvious yield point, an offset yield point is applied. The offset yield strength approach determines the elastic modulus and calculates the yield strength from where a specified offset at 2% strain parallel to the slope intercepts the stress-strain curve (Hahn, 1962). According to the power-function relationship, the yield strength in a quasistatic state ($\dot{\varepsilon} \to 0$) is equal to 1.45 GPa in the heterostructured $Al_3CoCrCuFeNi$ HEA.

The microstructural evolution of the heterostructure $Al_3CoCrCuFeNi$ HEA at the strain rate of 1×10^9 s^{-1} is presented in Fig. 3. The dominant development of deformation twinning is revealed. Higher magnification images show how twin embryo nucleates from a grain boundary (Fig. 4a) and then propagates towards the opposite grain boundary (Fig. 4b). With increasing the strain, the twin vertically grows via the slipping of 1/6<111> twinning dislocations on the {1 1 2} plane (Fig. 4c). Finally, the deformation twin expands laterally to cross the whole grain (Wang et al., 2015; Zhang et al., 2012; Li et al., 2020c; Li et al., 2017). The BCC to FCC phase transformation and the BCC to HCP phase transformations also take place during deformation due to the high lattice distortions around Al atoms (Lee et al., 2017; Jin et al., 2018). The observations of multiple phase transformations are unlike to the traditional BCC alloys, where dislocation slip and twinning are the only available deformation mechanisms.

Figure 5 clearly shows the strain-rate-dependent deformation behavior in the heterostructured $Al_3CoCrCuFeNi$ HEA. Dislocation slip and deformation twinning are the controlling deformation mechanisms at strain rates $< 1 \times 10^8$ s^{-1}. With increasing the strain rate, the nucleation of the twinning dislocation on adjacent (112) planes is observed, resulting in the increase width of the twin band through the layer-by-layer vertical growth (Fig. 5). In the BCC TiZrHfNbTa HEA, the nanoscale twin bands are found after cryogenic tensile deformation and are believed to be the reason for the improvement of the strain hardening capacity (Wang et al., 2020). When the strain rate is 1×10^9 s^{-1}, the deformation twinning together with multiple phase transformations (BCC to FCC, and BCC to HCP) occurs. When the strain rate is increased to 1×10^{10} s^{-1}, the BCC to FCC and BCC to HCP phase transformations become the main plastic deformation mode. The nucleation of FCC and HCP phases occurs at the triple junction, and then the discrete FCC and HCP nuclei are interconnected to form the large FCC and HCP particles (Fig. 6).

To clearly describe the evolution of the microstructure, the volume fractions of the deformation twins, FCC and BCC phases, are

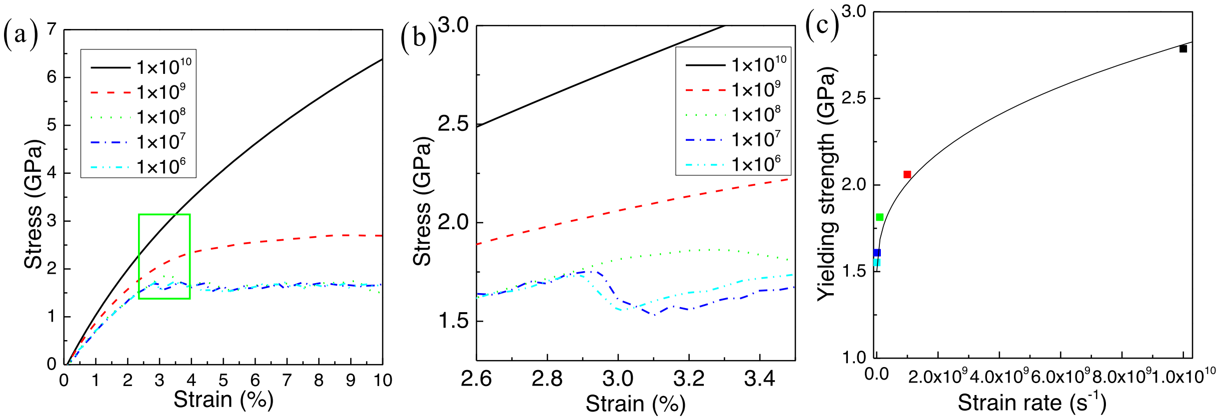

Fig. 2. The relationship between the stress and strain at different strain rates (a), and the corresponding local amplification of stress and strain (b). Variation of the yield strength and strain rate, and the corresponding fitting curve (c) of the heterostructured $Al_3CoCrCuFeNi$ HEA.

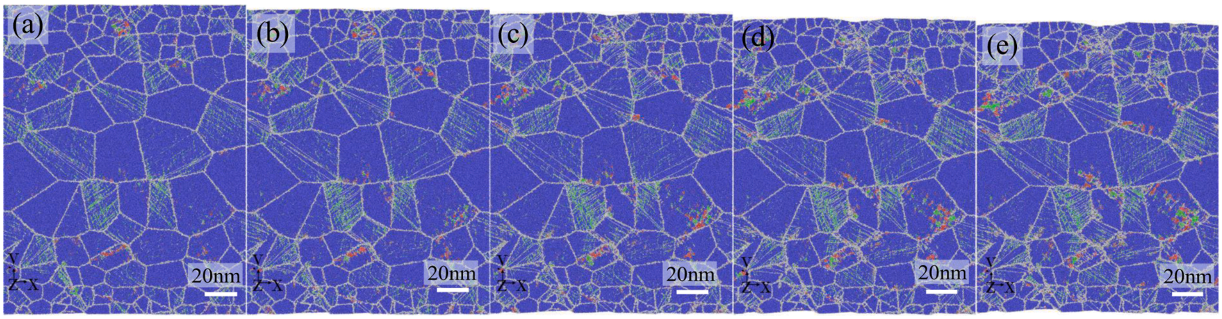

Fig. 3. The microstructure at the strain rate of 1 × 10^9 $s^{-1}$and different strains: 5% (a), 6% (b), 7% (c), 8% (d), and 9% (e).

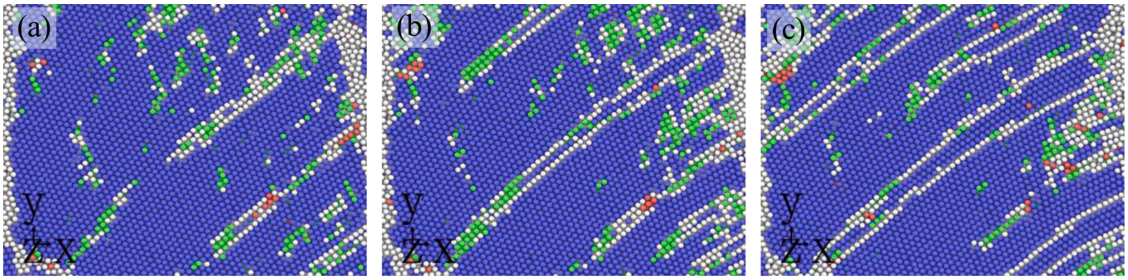

Fig. 4. (a) The nucleation of twin embryo, (b) growth of twin embryo, and (c) formation of a full twin plate at the strain rate of 1 × 10^9 s^{-1}.

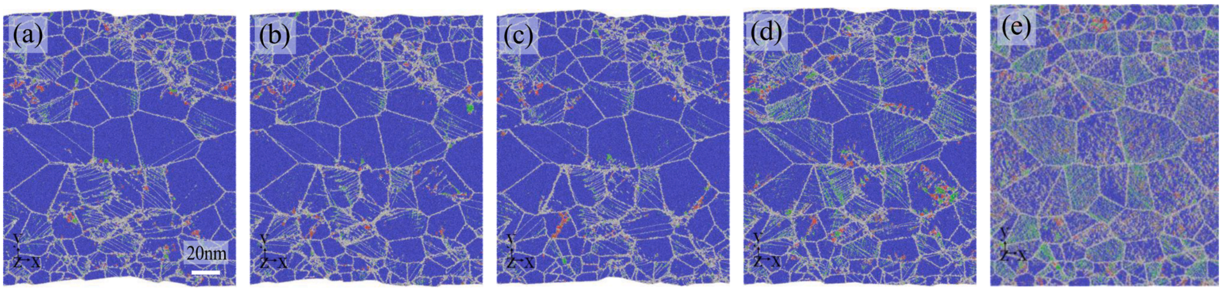

Fig. 5. The microstructure at the strain of 10% and different strain rates: 1 × 10^6 (a), 1 × 10^7 (b), 1 × 10^8 (c), 1 × 10^9 (d), and 1 × 10^{10} s^{-1} (e).

plotted in Fig. 7. The deformation twinning takes place at the relative low strain rate, such as 1 × 10^8 s^{-1}. Higher strain rates intensify phase transformations. Recently, the BCC to HCP phase transformation was found to enhance the strain hardening and ductility of a Ta0.5HfZrTi HEA, designed using "metastability engineering" approach (Huang et al., 2017; Wang et al., 2020), and the two-step phase transformations from the BCC to FCC structure impart significant plasticity and strain hardening of a BCC FeMnCoCr-based interstitial HEA (Tsianikas et al., 2021). Thus, our observations of multiple phase transformations further deepen the understanding of the deformation behavior in the heterogeneous HEA.

In addition, the evolution of the twin thickness with the increase of strain under different strain rates can be quantificationally observed from Fig. 8. When the strain reaches 3%, deformation twins gradually form at the strain rates of 1 × 10^6 s^{-1} and 1 × 10^7 s^{-1} in the grain size from 21 nm to 35 nm (Figs. 8a, b). However, the twin formation is delayed at the strain rates of 1 × 10^8 s^{-1} and 1 × 10^9 s^{-1}. The twin thickness is lower at the strain rate of 1 × 10^9 s^{-1}, compared with the case of the strain rates <1 × 10^8 s^{-1} (Figs. 8c, d), because the phase transformations become the main deformation mode. Moreover, the evolution of twin thickness in the large grains is obvious. The average twin thickness increases monotonously with the increase of strain in the grains with the size of 36-45 nm. However, the twins are much thinner and evolve slower in the finer grains. Hence, the current result not only reflects the effect of strain rate on plastic deformation, but also clearly shows the effect of grain size on the deformation twinning.

Figure 9 shows the spatial distributions of the stress and strain at various strain rates. The uneven distribution of strain/stresses, strongly affected by the strain rate, can be observed. The high tensile stresses are associated with the grain boundary regions at the strain rates <1 × 10^8 s^{-1}, while at higher strain rates (≥1 × 10^9 s^{-1}) stresses propagate toward the grains' interiors (Figs. 9a-e).Here, the width of a shear band is less than 1 nm (this situation is described as a "small shear band"), ranging from 1 to 3 nm (a medium shear band), and larger than 3 nm (a large shear band). By comparing the distribution of strains(Figs. 9f-j), it has been revealed the presence

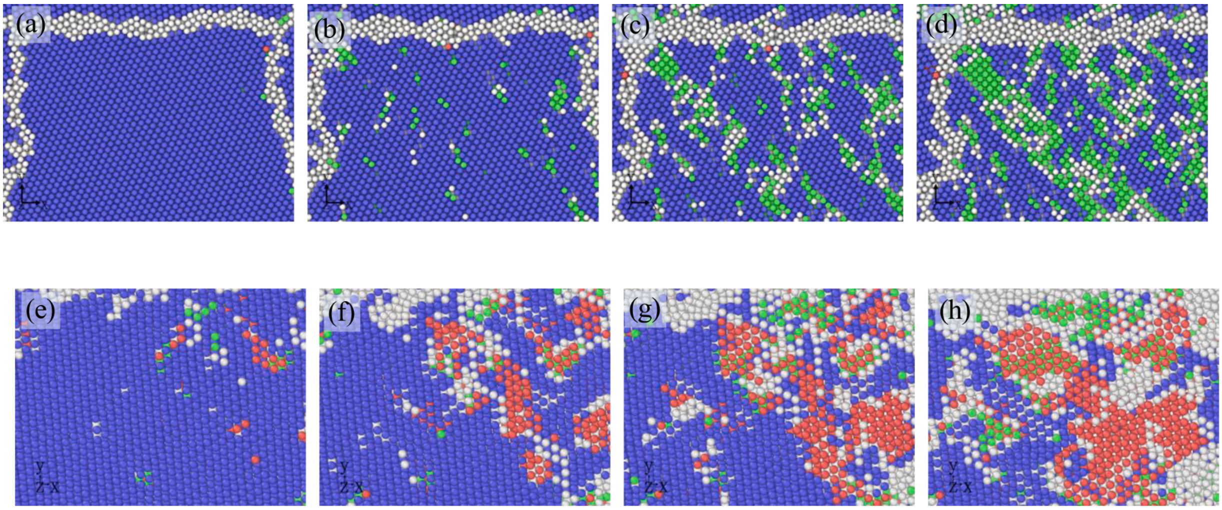

Fig. 6. The BCC to FCC phase-transformation process with the increased strain: 2% (a), 5.5% (b), 8% (c), and 10% (d) at the strain rate of 1 × 10^{10} s^{-1}. The BCC to HCP phase-transformation process with the increased strain: 5% (e), 7% (f), 8% (g), and 10% (h) at the strain rate of 1 × 10^{10} s^{-1}.

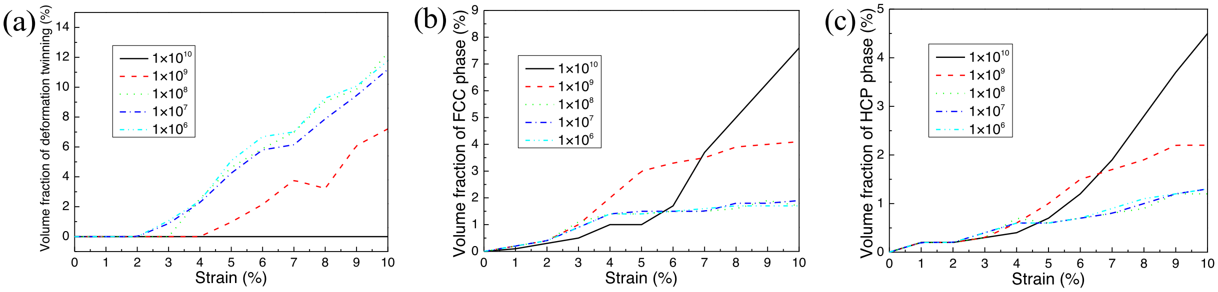

Fig. 7. The volume fractions of the deformation twin (a), FCC phase (b) and HCP phase (c) in the heterostructured Al_3CoCrCuFeNi HEA depending on the plastic strain.

of multiple shear bands. The appearances of the shear bands are almost identical at the strain rates ≤ 1 × 10^9 s^{-1}. On the contrary, lower number of thinner shear bands are observed at the strain rate of 1 × 10^{10} s^{-1}.

Figure 10 shows the variation of the stress and strain along the y axis in the HEA sample (see Fig. 9) for different strain rates. The average strain/stress is obtained by dividing the heterostructured Al_3CoCrCuFeNi HEA sample divided into 200 regions with the same width along the y direction and calculating the ratio between the sum of every atom strain/stress to the corresponding number of atoms in each region (Li et al., 2019; Fang et al., 2018). The strain and stress gradients are obviously observed in the Al_3CoCrCuFeNi HEA heterostructure. The increasing strain rate enhances the stress gradient effect, and reduces the strain gradient effect. Moreover, the stress/strain gradient distribution maybe come from the superimposed contributions of four aspects, which include the local severe lattice distortion, gradient grain size, deformation twinning, and phase transformation (Li et al., 2020c, 2020; L. Li et al., 2020b; L Li et al., 2020b). In turn, these multistage strengthening mechanisms from solute strengthening to phase transformation strengthening strongly affect the deformation behavior. Especially, the average local stress/strain jump is captured, which is different from the smooth stress distribution in traditional alloys (Li et al., 2019; Fang et al., 2018). Here, the local severe lattice distortion can be regarded as an atomic scale deformation unit to coordinate the local plastic deformation.

The dislocation characteristics and density are largely responsible for the mechanical response of the BCC HEAs (Aitken et al., 2019; Wang et al., 2020; Lee et al., 2020; Xu et al., 2021; Chen et al., 2020; Wang et al., 2020; Maresca and Curtin, 2020; Lee et al., 2021; Eleti et al., 2020, 2021). From Fig. 11a, the dislocation density is weakly affected by the strain rate change in the range 1 × 10^6 - 1 × 10^8 s^{-1}, but decreases rapidly with the further increase of the strain rate. This trend agrees well with the deformation mechanism changes with the increasing strain rate discussed above. The results obtained also show that the edge dislocations prevail in comparison with the screw dislocations (Fig. 11b). Excluding the contributions of the grain boundary and twinning to the strength, the edge character dislocations would greatly affect the work hardening. On the other hand, the massive 1/2<111> dislocations can enhance the plasticity (Fig. 11c), similarly to the other BCC alloys and metals under the tensile deformation (Li et al., 2019; Fang et al., 2018).

The similarities and differences of dislocation behavior between our atomic simulations and experiments would be discussed. The non-screw dislocations have been observed in previous experiments (Wang et al., 2020; Lee et al., 2020), which correlates well with

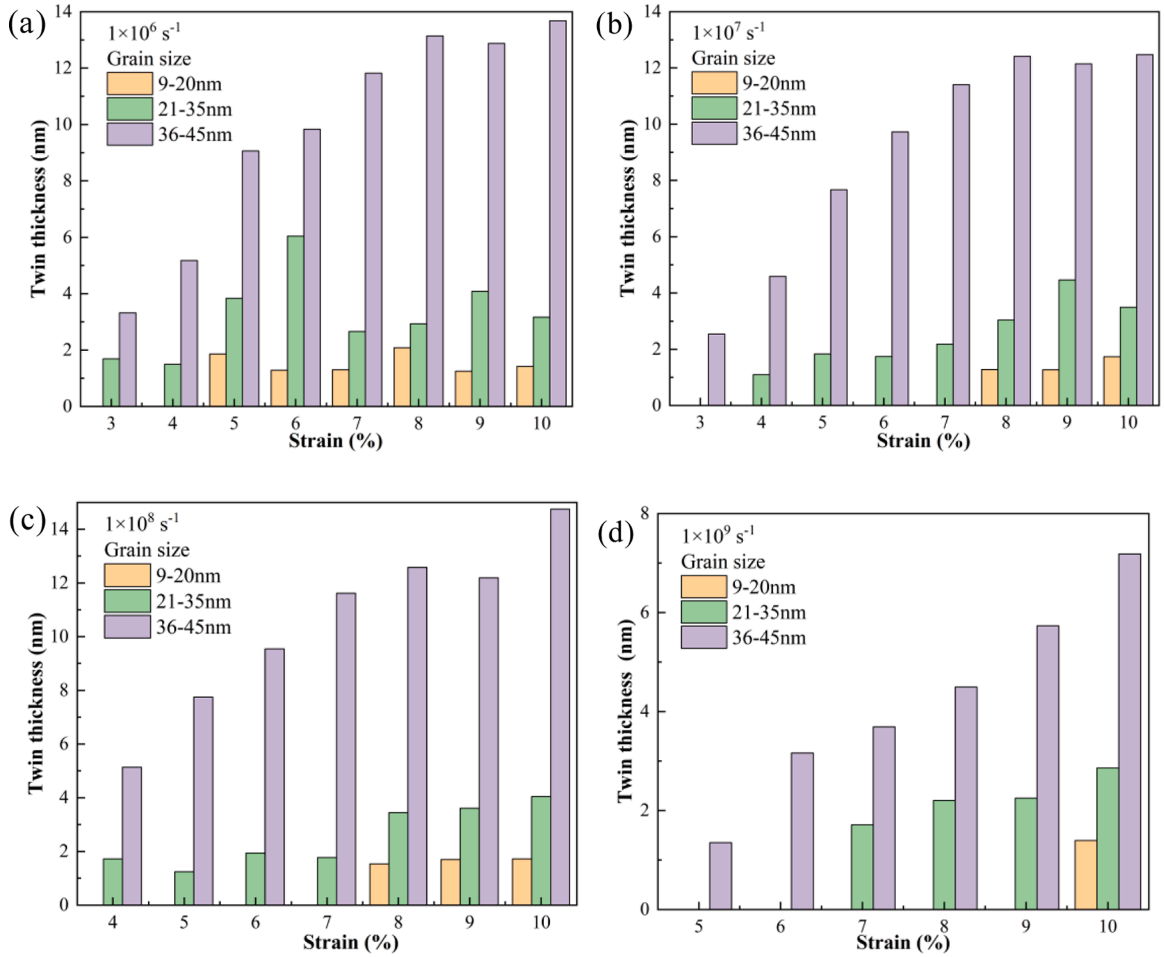

Fig. 8. The evolution of the twin thickness at different strain rates: 1 × 10^6 (a), 1 × 10^7 (b), 1 × 10^8 (c), and 1 × 10^9 s^{-1}(d). The orange bar denotes the twin thickness at grain sizes from 9 nm to 20 nm, the green bar is the twin thickness at grain sizes from 21 nm to 35 nm, and the purple bar represents the twin thickness at grain sizes from 36 nm to 45 nm of the heterostructured $Al_3CoCrCuFeNi$ HEA.

the present MD simulation results (Fig. 11b). For example, the unexpected dominance of non-screw dislocations and numerous slip planes activated leads to a desirable combination of the homogeneous plastic flow and high strength in MoNbTi alloys (Wang et al., 2020), and the <111> {110} edge dislocations mediated plastic deformation in the BCC NbTaTiV HEA, as captured by high-angle annular dark-field scanning transmission electron microscopy (Lee et al., 2020). The dislocation character at different strain rates would affect the work-hardening abilities of the HEA under quasi-static and dynamic deformation (Zhang et al., 2017; He et al., 2020). From the previous experimental work (Zhang et al., 2017; He et al., 2020), the dislocation slip is the dominant deformation mechanism at the quasi-static strain rates, and stacking faults or mechanical twinning mediate the dynamic deformation. The current results are relatively consistent with the above reports. However, the present result also shows that the phase transformations can contribute to the work hardening behaviour at the extremely high strain rates. In addition, for the dislocation networks formed, the parallel distribution of relative aggregation of dislocations is close to the grain boundary (Fig. 11c), which is different from the dislocation tangle in the HEA (Huang et al., 2021; Ma et al., 2015; Li et al., 2017). This trend would be attributed to the columnar nano-grain sample, which suppresses more slip system activation.

4. Theoretical modeling

Based on the analysis of the uniaxial tensile-mechanical behavior by the MD simulation in the previous section, a microstructure-based constitutive model that utilizes a single parameter set is proposed to quantitatively describe the tensile stress-strain response of the heterostructured $Al_3CoCrCuFeNi$ HEA. The grain size of the gradient nano-polycrystalline structure ranging from 9 nm on the surface to 45 nm at the center of the structure is constructed, which is consistent with the model in MD simulations, as shown in Fig. 12.

The elastic-strain rate and plastic-strain rate form the total strain rate:

$$\dot{\boldsymbol{\varepsilon}} = \dot{\boldsymbol{\varepsilon}}_e + \dot{\boldsymbol{\varepsilon}}_p \tag{1}$$

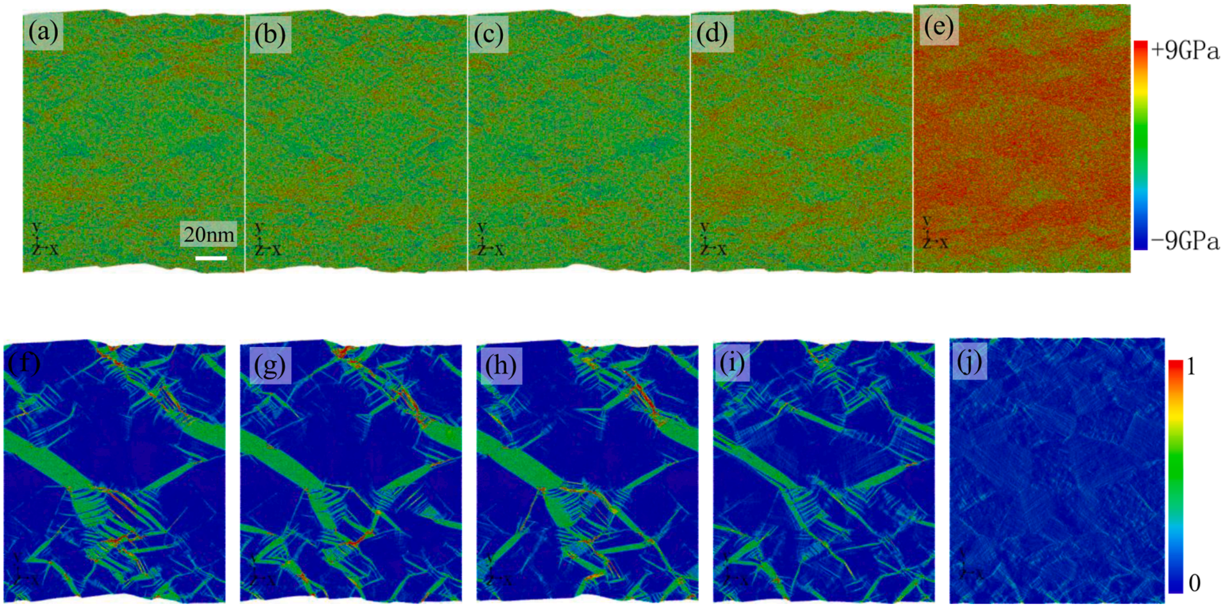

Fig. 9. The stress distribution at the strain of 10% and different strain rates: 1 × 10^6 (a), 1 × 10^7 (b), 1 × 10^8 (c), 1 × 10^9 (d), and 1 × 10^{10} s^{-1} (e). The strain distribution at the strain of 10% and different strain rates: 1 × 10^6 (f), 1 × 10^7 (g), 1 × 10^8 (h), 1 × 10^9 (i), and 1 × 10^{10} s^{-1} (j).

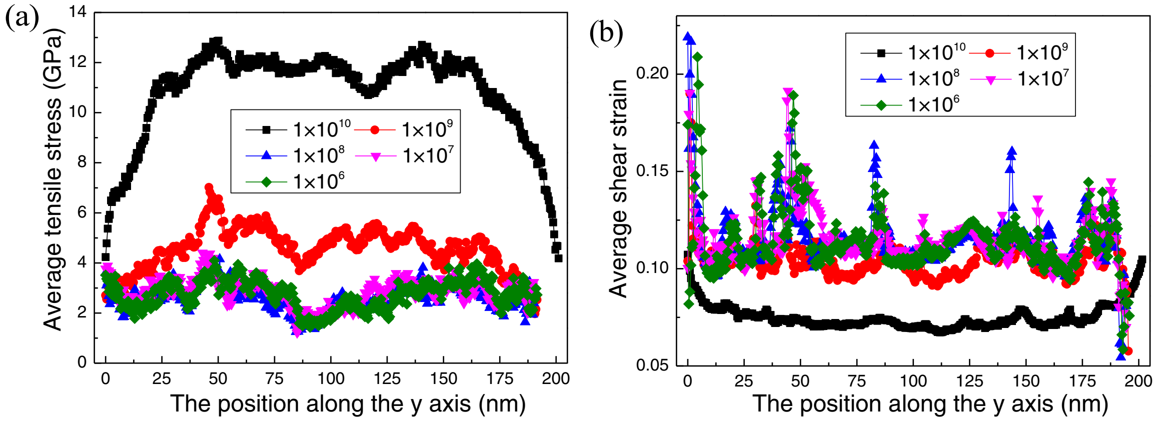

Fig. 10. Distribution of the axial stress gradient (a) and shear strain gradient (b) along the y axis at the applied strain of 10% of the heterostructured $Al_3CoCrCuFeNi$ HEA.

The elastic part conforms to Hooke's law:

$$\dot{\boldsymbol{\varepsilon}}_e = \mathbf{M} : \dot{\boldsymbol{\sigma}} \tag{2}$$

where **M** is the elastic compliance tensor, and $\dot{\boldsymbol{\sigma}}$ is the stress rate tensor, which represents the differentiation of the stress tensor with respect to time.

The plastic strain rate can be expressed as:

$$\dot{\boldsymbol{\varepsilon}}_p = \frac{3}{2}\frac{\dot{\varepsilon}_p}{\sigma}\boldsymbol{\sigma}' \tag{3}$$

where $\boldsymbol{\sigma}' = \sigma_{ij} - \sigma_{kk}\delta_{ij}/3$ denotes the deviatoric stress tensor, $\dot{\varepsilon}_p = \sqrt{2\dot{\varepsilon}_{p_{ij}}\dot{\varepsilon}_{p_{ij}}/3}$ means the Von Mises equivalent plastic strain rate, $\sigma = \sqrt{3\sigma'_{ij}\sigma'_{ij}/2}$, is the Von Mises equivalent stress.

The relationship between the equivalent plastic strain rate and equivalent stress is:

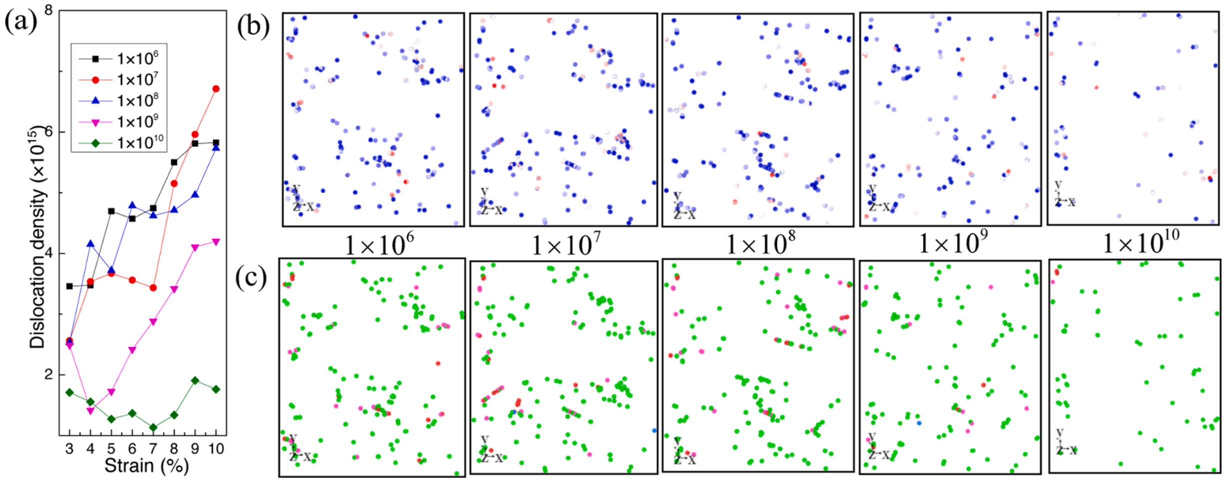

Fig. 11. Dislocation density depending on the strain after yielding at different strain rates in the heterostructured $Al_3CoCrCuFeNi$ HEA (a). The edge/screw dislocation distributions at the strain of 10% and different strain rates (b). The blue lines stand for the edge dislocations, the red lines stand for screw dislocations, and other color lines stand for the mixed dislocations. The different types of dislocation distributions at the strain of 10% and different strain rates (c), where the 1/2<111> (green line), <100> (pink line), <110> (blue line), and other (red line) dislocations.

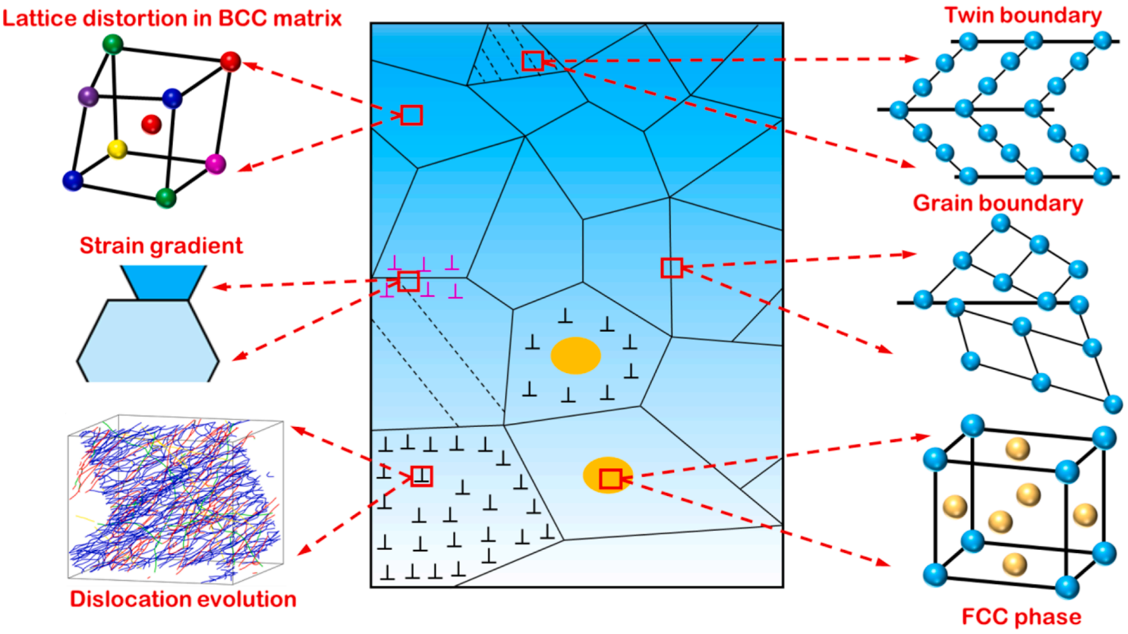

Fig. 12. The schematic illustration of the existing microstructure in the heterostructured Al3CoCrCuFeNi HEA, including the lattice distortion of the BCC matrix, dislocation evolution, deformation twin, grain boundary, strain gradient, and phase-transformation-induced FCC or HCP phases.

$$\dot{\varepsilon}_p = \dot{\varepsilon}\left(\frac{\sigma}{\sigma_{\text{flow}}}\right)^m \tag{4}$$

where $\dot{\varepsilon} = \sqrt{2\dot{\varepsilon}'_{ij}\dot{\varepsilon}'_{ij}/3}$ represents the equivalent strain rate, $\dot{\varepsilon}'_{ij} = \dot{\varepsilon}_{ij} - \dot{\varepsilon}_{kk}\delta_{ij}/3$. m is the sensitivity factor of rate, and σ_{flow} is the flow stress.

In view of the microstructure evolution at various strain rates from MD simulations, all the existing strengthening mechanisms should be integrated into the constitutive model, as presented in Fig. 12. The total flow stress can be expressed as:

$$\sigma_{\text{flow}} = \sigma_{\text{GB}} + \sigma_{\text{d}} + \sigma_{\text{f}} + \sigma_{\text{b}} + \sigma_{\text{twin}} + \sigma_{\text{phase}} \tag{5}$$

where σ_{GB} is the grain-boundary strengthening, σ_d is dislocation strengthening, σ_f is the lattice-friction stress deriving from the severe lattice distortion in HEAs, σ_b is the back stress strengthening, σ_{twin} is the twinning strengthening, and σ_{phase} is the phase-transformation strengthening.

The contribution from the grain-boundary strengthening to the flow stress can be expressed as:

$$\sigma_{\mathrm{GB}} = \frac{k_{\mathrm{HP}}}{\sqrt{d}} \tag{6}$$

where k_{HP} is a Hall-Petch coefficient.

The dislocation strengthening can be expressed as:

$$\sigma_{\mathrm{d}} = M\alpha\mu b\sqrt{\rho} \tag{7}$$

where M, α, μ, b, and ρ are the Taylor factor, Taylor constant, shear modulus, magnitude of Burgers vector, and dislocation density, respectively. According to the Kocks-Mecking model (Kocks and Mecking., 2003) the proliferation and annihilation of the dislocation density inside grains can be expressed as:

$$\frac{d\rho}{d\varepsilon_p} = M\left(k + k_1\sqrt{\rho} - k_2\rho\right) \tag{8}$$

where $k = \frac{1}{bd}$, $k_1 = \frac{\psi}{b}$, $k_2 = k_{20}\left(\frac{\dot{\varepsilon}_p}{\dot{\varepsilon}_0}\right)^{-\frac{1}{n_0}}$, ψ is the proportionality factor, k_{20} is the dynamic annihilation constant-independent of size, and $\dot{\varepsilon}_0$ is the reference strain rate.

The back stress can be divided into the intragranular one and intergranular one. The former one is ignored due to the lack of the heterogeneous dislocation distribution in the nano-grains. The intergranular is produced by the plastic strain incompatibility between grains, which is considered in our work. The geometrically necessary dislocations (GNDs) would be generated to accommodate the strain incompatibilities. The contribution of the back stress can be expressed as:

$$\sigma_b = M\frac{\mu b}{d}N \tag{9}$$

where N represents the number of GNDs accumulated at the grain boundary.

The evolution law of the number of GNDs is:

$$\frac{dN}{d\varepsilon_p} = \frac{\zeta}{b}\left(1 - \frac{N}{N_*}\right) \tag{10}$$

where ε_p is the plastic strain, ζ is the mean interval between slip bands, and N_* is the maximum number of pileup dislocations at the grain boundary.

The deformation twinning strengthening depends upon the critical twin thickness (Wei, 2011). The contributed stress from the deformation twins can be expressed as:

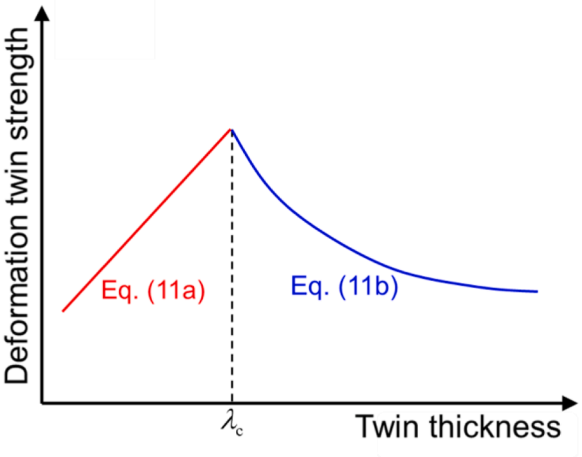

Fig. 13. The schematic diagram of the deformation twin strength vs. twin thickness. Here, the red line is obtained by Eq. (11a), and the blue line is determined based on the Eq. (11b). λ_c is the critical twin thickness.

$$\sigma_{\text{twin}} = \begin{cases} M\left(\tau_l + \chi\mu\frac{\pi}{8}\frac{2-\upsilon}{1-\upsilon}\frac{\lambda}{d}e^T + \varphi\frac{\gamma_{\text{tb}}}{\lambda e^T}\right), \lambda \le \lambda_c(\text{a}) \\ M\frac{1}{n}\left(\frac{\gamma_{\text{sf}}}{b_{\text{p}}} + \frac{\mu b}{3\lambda}\right), \lambda > \lambda_c(\text{b}) \end{cases} \tag{11}$$

where τ_l is the lattice resistance to the motion of twinning partials in a twin plane, χ is a coefficient on the order of unit, υ is Poisson's ratio, λ is the twin thickness, e^T is the transformation shear strain, φ is a coefficient dependent on the forming process of a twin boundary, γ_{tb} is the twin stacking fault energy, n is a geometrical parameter, γ_{sf} is the stacking fault energy, and b_p is the Burgers vector of a partial dislocation. Here, $\varphi = -2$ represents the complete detwinning of a twin boundary, $\varphi = 2$ denotes the formation of a twin boundary, and $\varphi = 0$ represents the thickening or thinning of a twin boundary. The MD simulations suggest that the thickening of a twin boundary continuously takes place during the deformation stage (Fig. 8), and thus, φ is equal to 0 in our work. Although Eq. (11) is employed to describe the deformation twinning strengthening in FCC alloys, the model of BCC HEAs still lacks. Thus, a more appropriate deformation twinning strengthening model needs to be put forward in BCC HEAs.

Here, based on Eq. (11), the deformation twinning strengthening increases and then decreases with increasing the twin thickness. The relationship between the twin thickness and twinning strengthening has an intersection point, which corresponds to the maximum deformation twinning strengthening and the critical twin thickness (Fig. 13). Based on the MD simulation, the critical twin thickness ranges from 2.0 to 6.9 nm, which depends on the grain size from 9 to 45 nm. In the constitutive model, twin-thickness evolution is consistent with the result of MD simulation in Fig. 8. Thus, in accordance with the evolution of deformation twin thickness, the deformation twinning strengthening in the constitutive model is determined, and accurately predicts the mechanical properties at different strain rates.

The present work focuses on the microstructure-based mechanical properties. The parameters of the microstructure evolution are taken from our MD simulation, and the geometrical parameters are from the previous work (Wei, 2011). Furthermore, the effect of the geometric parameters on the twin-boundary strengthening was tested through trial and error. It is found that the obvious geometric parameter change (increasing or reducing them by doubling) hardly affects the predicted results. Therefore, the influence of the geometric parameters on the mechanical properties is ignored.

The contributed stress from the phase interface is dependent on the size and volume fraction of the multiple phase transformation-induced FCC and HCP phases. Here, the modified Hall-Petch formula is employed to calculate the phase strengthening, which can be written as:

$$\sigma_{\text{phase}} = \left\{ \frac{\frac{2f_{\text{FCC}}k_{\text{FCC}}}{\sqrt{d_{\text{FCC}}}}}{\frac{2f_{\text{FCC}}k_{\text{FCC}}}{\sqrt{d_{\text{HCP}}}}} \right. \tag{12}$$

where f_{FCC} and f_{HCP} are the volume fractions of the FCC and HCP phases, respectively. k_{FCC} and k_{HCP} are the FCC phase-interface strengthening coefficient and HCP-phase-interface-strengthening coefficient, respectively. d_{FCC} and d_{HCP} are the sizes of the FCC and HCP phases, respectively.

The response between the stress and strain of the heterostructured Al_3CoCrCuFeNi HEA is described by Eqs. (1-12). Due to the gradient variation of grain sizes from the surface to the inside of the structure, the rule of mixtures is used to express the total flow stress of the heterostructured Al_3CoCrCuFeNi HEA, which consists of n phases as presented in Fig. 14 (Li et al., 2017; Li et al., 2020c). The total stress is then expressed as:

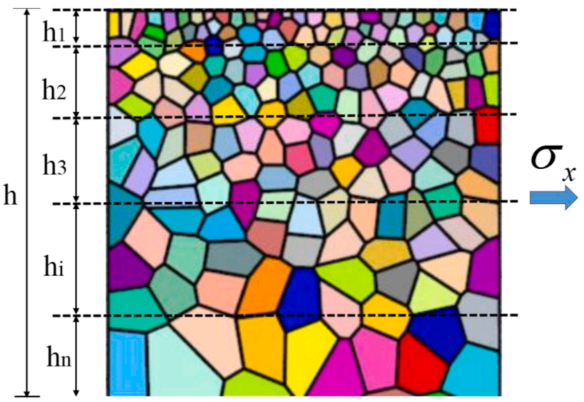

Fig. 14. The heterostructured Al_3CoCrCuFeNi HEA is assumed to be a composite structure with n phases. The larger the value of n, the more accurate the calculation.

$$\sigma_x = \left(\sum_{i=1}^{n} \sigma_{xi} h_i\right) \Big/ h \tag{13}$$

where the σ_{xi} and h_i are the stress and thickness of the i phase, respectively. h is the thickness of the whole heterostructure.

It is necessary to emphasize that all the present parameters in the microstructure-based constitutive model are from our MD simulation results and the previous experiments, and include the empirical parameters and physical parameters determined by the material itself. These parameters compose a single parameter set, which can be applied to the subsequent calculations at all the different strain rates without further adjustment in the present work. The Hall-Petch coefficient, $k_{\mathrm{HP}} = 0.216$ MPa m$^{1/2}$, is determined by the weighted mean method based on the previous research (Sriharitha et al., 2014). The Taylor factor, M, is 3.06 (Ganji et al., 2017), and the Taylor constant, α, is 0.33 (Zhu et al., 2011; Li et al., 2012). The shear modulus and Burgers vector are obtained from the MD simulation. The lattice-friction stress is determined by fitting the MD simulation, which is considered to be a fixed value at different strain rates. For the twin-boundary strengthening, the lattice resistance to the motion of twinning partials in a twin plane, τ_l, is on the order of the lattice-friction stress. Here, τ_l is assumed to be equal to σ_{f}/M. The transformation shear strain, e^T, the coefficient, φ, the coefficient, χ, and the geometrical parameter, n, are extracted from the previous work (Wei, 2011). The twin stacking fault energy, γ_{tsf}, and the stacking fault energy, γ_{sf} are acquired from our MD simulation, which are 717 mJ / m^2 and 674 mJ / m^2, respectively. For the multiple phase-transformations strengthening, the volume fractions f_{FCC}, f_{HCP} of FCC and HCP phases, and the sizes d_{FCC} and d_{HCP}, of FCC and HCP phases are taken from our MD simulation, as shown in Fig. 7. All the parameters are summarized in Table 1.

Thus, based on the atomic-simulation result and Eqs. (5-13), the stress-strain curves of the heterostructured Al_3CoCrCuFeNi HEA can be predicted. The specific steps of the numerical method are described as follows:

(I) Firstly, defining the constitutive parameters values in Eqs. (5-13). To initialize the dislocation density, here, ρ_0 is 3×10^{12} m^{-2} (Xu et al., 2018). To initialize the number of GNDs accumulated at the grain boundary, and N_0 is equal to 0.

(II) Secondly, to calculate the plastic-strain-rate tensor, elastic-strain-rate tensor, the dislocation density, $\dot{\rho}(t_{\mathrm{n}})$, and the number of GNDs accumulated at the grain boundary, $\dot{N}(t_{\mathrm{n}})$, at the time step, t_{n} (n = 1, 2…). To calculate the grain-boundary strengthening, σ_{GB}, the deformation twin strengthening, σ_{twin}, the phase strengthening, σ_{phase}, the lattice-friction stress, σ_{f}, the dislocation strengthening, σ_{d}, and the back stress, σ_{b} at the time step, t_{n} (n = 1, 2…) based on Eqs. (6, 7, 9, 11, and 12). To calculate the flow stress, σ_{flow}, at the time step, t_{n} (n = 1,2…), according to Eq. (5).

(III) Thirdly, updating the values of stress and strain at the time step, t_{n} (n = 1, 2…).

(IV) Then, to calculate the corresponding values of the microstructure at a time step, $t_{\mathrm{n+1}}$ (n = 1, 2…), according to the time increment method, such as $\rho(t_{\mathrm{n+1}}) = \rho(t_{\mathrm{n}}) + \dot{\rho}(t_{\mathrm{n}})\Delta t$.

(V) Lastly, to recall the steps II to Ⅳ, until the strain reaches 6%.

Table 1
Constitutive parameters of the heterostructured Al_3CoCrCuFeNi HEA.

Parameter	Symbol	Magnitude
Grain size (nm)	d	9-45
Shear modulus (GPa)	μ	30
Poisson's ratio	υ	0.3
Burgers vector of complete dislocation (nm)	b	0.25
Hall-Petch constant (MPa m$^{1/2}$)	k_{HP}	0.216
FCC phase interface strengthening coefficient (MPa m$^{1/2}$)	k_{FCC}	0.236
HCP phase interface strengthening coefficient (MPa m$^{1/2}$)	k_{HCP}	0.290
Empirical constant	α	0.33
Taylor factor	M	3.06
Dynamic recovery constant	n_0	21. 5
Proportionality factor	ψ	0.025
Dynamic recovery constant	K_{20}	21.25
Maximum number of dislocations	N_*	10
Mean spacing between slip bands (nm)	ζ	1
Lattice resistance (MPa)	τ_l	45.7
The transformation shear strain	e^T	0.707
Reference strain rate (s^{-1})	$\dot{\varepsilon}_0$	1
Twin stacking fault energy (mJ / m^2)	γ_{tsf}	717
Stacking fault energy (mJ / m^2)	γ_{sf}	674
Coefficient	χ	0.4
Geometrical parameter	n	1.8
Burgers vector of partial dislocation (nm)	b_p	0.149
Initial dislocation density (m^{-2})	ρ_0	3×10^{12}
Initial GNDs density (m^{-2})	N_0	0

It is worth noting that the change of the dislocation density in the tensile process is used to decide whether plastic deformation in the model starts, which is in line with the MD-simulation result. The flowchart of computational process is shown in Fig. 15.

Figures 16a and 16b compare the stress-strain curves from the MD simulation and the microstructure-based constitutive model at strain rates of 1×10^8 s^{-1} and 1×10^9 s^{-1}, which are selected because of the different deformation mechanisms. The red lines represent the total stress-strain response deriving from the individual mechanisms in Figs. 16a and 16b. At the strain rate of 1×10^8 s^{-1}, there is a small deviation when the strain is greater than 5% in Fig. 16a. This trend is due to the effect of surface softening for the film tensile specimen in MD simulations (Chen et al., 2019). Here, this phenomenon would not be considered in the constitutive model, due to that the softening mechanism is complex, and its effect on strength can be ignored before large plastic deformation. In addition, our model prediction agrees well with the MD simulation before the softening stage. At the strain rate of 1×10^9 s^{-1}, the excellent agreement is acquired in both elastic and plastic stages. It is revealed that the present model is reliable enough to predict the mechanical behavior by integrating the microstructure evolution into the multistage strengthening mechanisms. It is noted that both the microstructure evolution and stress-strain responses at strain rates of 1×10^6 s^{-1}, 1×10^7 s^{-1}, and 1×10^8 s^{-1} are similar to the MD simulations. Therefore, we only calculate the mechanical behavior at a strain rate of 1×10^8 s^{-1}.

Figures 16a and 16b also illustrate the comparison of the stresses contributed from various mechanisms to the total strength with increasing strain. Here, dislocations, back stress, FCC/HCP phases, and deformation twinning mainly contribute to the strain hardening, since the densities of the FCC/HCP phase, dislocation, and deformation twin continuously increase. The contribution from the multiple-phase-transformations induced FCC/HCP structure at the strain rate of 1×10^9 s^{-1} is significantly larger than that at the strain rate of 1×10^8 s^{-1} (see Figs. 16a and 16b). The back stress at the strain rate of 1×10^9 s^{-1} is slightly larger than that at the strain rate of 1×10^8 s^{-1}. The deformation-twin strengthening at the strain rate of 1×10^9 s^{-1} is smaller than that at the strain rate of 1×10^8 s^{-1}. Therein, the dislocation strengthening exhibits an asymptotic behavior, which increases rapidly firstly, and then approaches a saturation value. The phase strengthening and back stress keep increasing as strain increases. The twin-boundary strengthening is absent when strain is less than 3%. Grain boundaries play an indispensable role in the total strength. Moreover, the nano-scale grain size influences the dislocation density in the grain interior based on Eqs. (7, 8). Therefore, changing the grain size would affect both the strength and strain hardening of the heterostructured Al_3CoCrCuFeNi HEA.

Figures 16c and 16d exhibit the contributed proportion from the multistage-strengthening mechanisms to the strain hardening. It is noted that grain-boundary strengthening and lattice-distortion strengthening keep constant at the onset of the plastic region (Figures 16a and 16b). Therefore, neither the grain boundary nor lattice distortion contributes to the strain hardening. At the strain rate of 1×10^8 s^{-1}, the dislocation multiplication controls the strain hardening at the initial stage of deformation. With strain increasing, the FCC/HCP phases and the deformation twinning would dominate the strain hardening. At the strain rate of 1×10^9 s^{-1}, the strain hardening relies on the FCC/HCP multiple phase transformations during plastic deformation. On the other hand, the contributions from dislocation, deformation twins, and back stresses are almost equivalent, and occupy 35% of the total strain hardening at strain of 6%. Thus, the contributed proportion from multiple mechanisms on the yield strength and strain hardening are quantitatively illustrated. Therefore, by integrating the multistage-strengthening mechanisms, the microstructure-based constitutive model that utilizes a single parameter set can capture the features of the variation in the stress-strain response. This current theoretical model still has some shortcomings for the prediction of the strain-stress curve at high strain rates and strains. In our constitutive model, various strengthening mechanisms are linearly superimposed, considering a weak coupling effect. However, various microstructures are highly simultaneous at high strain rates and strains in the MD simulations, resulting in the complex coupling effects of various strengthening mechanisms on the mechanical properties. Therefore, the present constitutive model agrees well with the MD-simulation results at small strains ($<$ 6%) and strain rates less than $< 1 \times 10^9$ s^{-1}.

The experimental research related to the effect of strain rate on twinning and phase transformation in heterostructured BCC HEAs is still scarce. In order to verify the constitutive model further, Fig. 17 shows the comparisons between the proposed constitutive model and experiment in other HEAs, which involve twinning and phase transformation as the main deformation mechanisms. Figure 17a exhibits differences in the stress-strain curves between our microstructure-based constitutive model and the previous experiment Fu et al., 2016). Here, the strength from experiment is 1,795 MPa, and the calculated strength is 1,818 MPa. The deviation of our model prediction is only 1.2%, indicating the universality of the constitutive model. Here, the grain-boundary strengthening and solid-solution strengthening are equal to the result of the experiment (Fu et al., 2016), where the grain-boundary strengthening is 1, 136 MPa, and the solid-solution strengthening is 28 MPa. In addition, the calculated dislocation strengthening is 622 MPa, based on the Eqs. (7-8), and the calculated deformation-twin strengthening is 32 MPa, based on Eq. (11).

Figure 17b shows the comparisons of the phase-transformation strengthening between the prediction and experiment (Zhang et al., 2020). The theoretical result is obtained, based on Eq. (12). The experiments indicate that the size of the transformation-induced phase increases from 30 nm to 200 nm with increasing the plastic strain to 35%. The volume fraction of the transformation-induced phase increases from 6.6% to 45.5%, which is approximately consistent with a linear change. Here, the size of the transformation-induced phase is assumed to be linearly increasing, the same as the situation of the volume fraction evolution. The results show that our constitutive model can capture the phase-transformation-induced strength with increasing the strain from the experiments. The theoretical model agrees better with the experiment, comparing to the MD simulations. The microstructure evolution is more complex in the MD simulations due to a high strain rate. In the experiment (Fu et al., 2016), grain boundaries dominate the yield strength, and dislocations controls the strain hardening, but deformation twins and solid-solution strengthening are neglected (Fig. 17a). In the experiment (Zhang et al., 2020), only the phase transformation dominates the strain hardening (see Fig. 17b). Therefore, based on the microstructure evolution, the present model can quantitatively predict the strength and reveal multistage strain hardening.

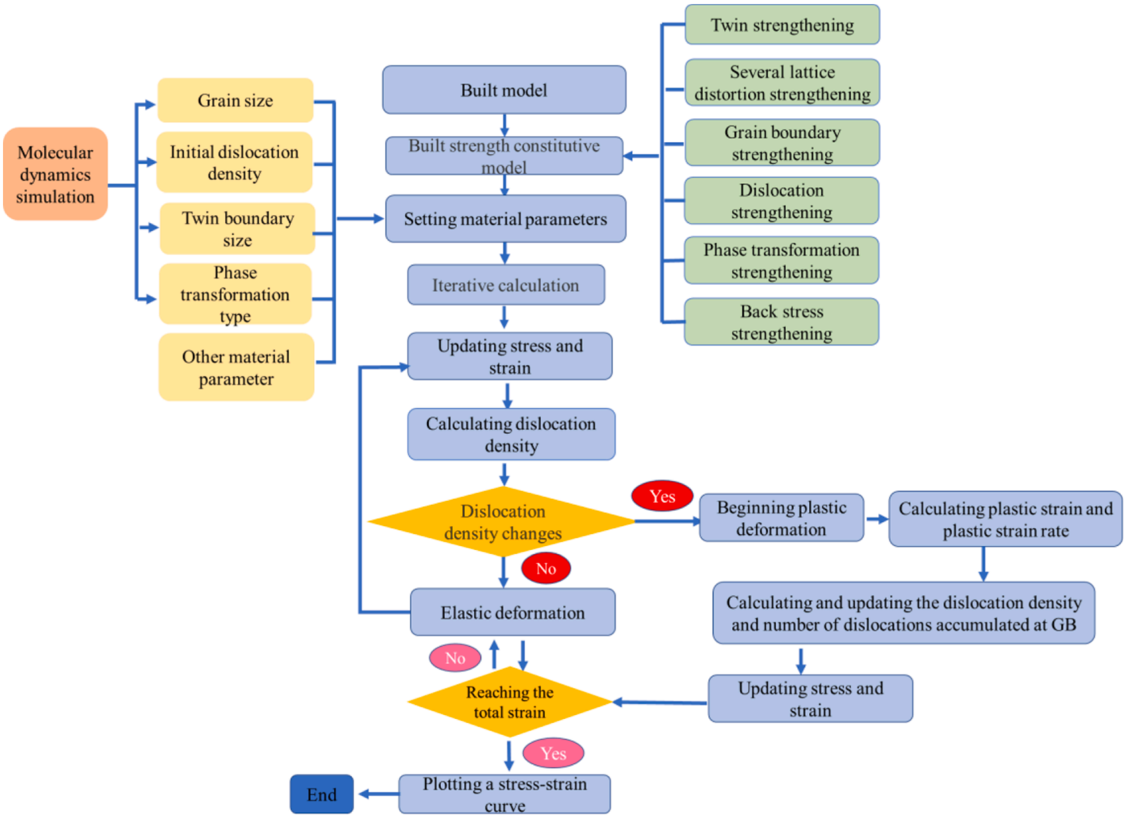

Fig. 15. The flow chart of the computational process for the stress-strain curve.

5. Conclusion

In the present work, the MD simulation method is used to study the rate-dependent deformation of the heterostructured $Al_3CoCrCuFeNi$ HEA under the uniaxial tension, and its mechanical response is observed from the atomic point of view. In the process of tensile deformation, the flow stress drops rapidly first, and then keeps stable with increasing strain. The atomic-simulation result reveals that when the loading strain rate is less than 1×10^8 s^{-1}, plastic deformation is controlled by dislocations and deformation twinning. As the strain rate further increases, deformation twinning and multiple phase transformations co-dominate during the plastic deformation at the strain rate is 1×10^9 s^{-1}. The model of the plastic-deformation response is associated with the multiple phase transformations at the strain rate of 1×10^{10} s^{-1}. In addition, massive edge dislocations dominate high strength, which are different from the classical generally-accepted view that screw dislocations are the origin of plastic flow in BCC metals and alloys. Subsequently, a microstructure-based constitutive model that utilizes a single parameter set is proposed to describe the stress-strain response of a heterostructured HEA by integrating the observed deformation mechanisms from the MD simulations. The predicted stress-strain curves exhibit excellent agreement with the MD-simulation results at different strain rates. The effects of different mechanisms on the yield strength and strain hardening are quantitatively illustrated. The grain-boundary strengthening and lattice-friction stress contribute to the yield strength, and dislocations, back stress, deformation twins, and phase transformation mainly contribute to the strain hardening. The atomic simulation and theoretical calculation provide the understanding of strain rate-dependent deformation mechanisms in a model heterogeneous HEA at the atomic scale.

Author statement

Jing Peng: Formal analysis, Software, Investigation, Data curation, Writing - original draft.
Li Li: Formal analysis, Software, Investigation, Data curation, Writing - original draft.
Fang Li: Investigation, Data curation, Validation.
Bin Liu: Visualization, Software.
Sergey Zherebtsov: Writing - review & editing.
Qihong Fang: Conceptualization, Validation, Writing - review & editing, Supervision, Funding acquisition.
Jia Li: Conceptualization, Methodology, Writing - review & editing, Supervision, Funding acquisition.
Nikita Stepanov: Writing - review & editing.

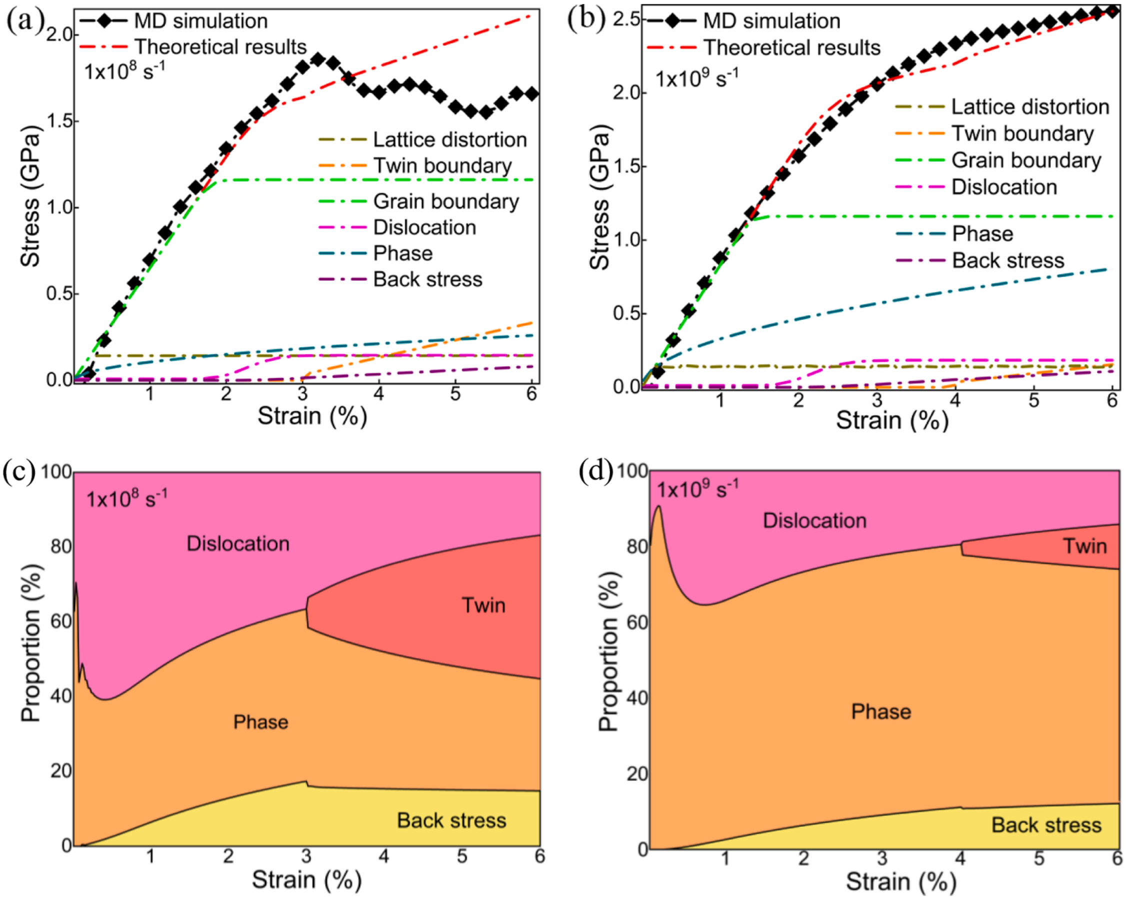

Fig. 16. The stress-strain response of heterostructured $Al_3CoCrCuFeNi$ HEA and the respective contributions from the multistage-strengthening mechanisms at strain rates of 1×10^8 s^{-1} (a) and 1×10^9 s^{-1} (b). The proportion of various strengthening mechanisms to the strain hardening at strain rate of 1×10^8 s^{-1} (c) and 1×10^9 s^{-1} (d).

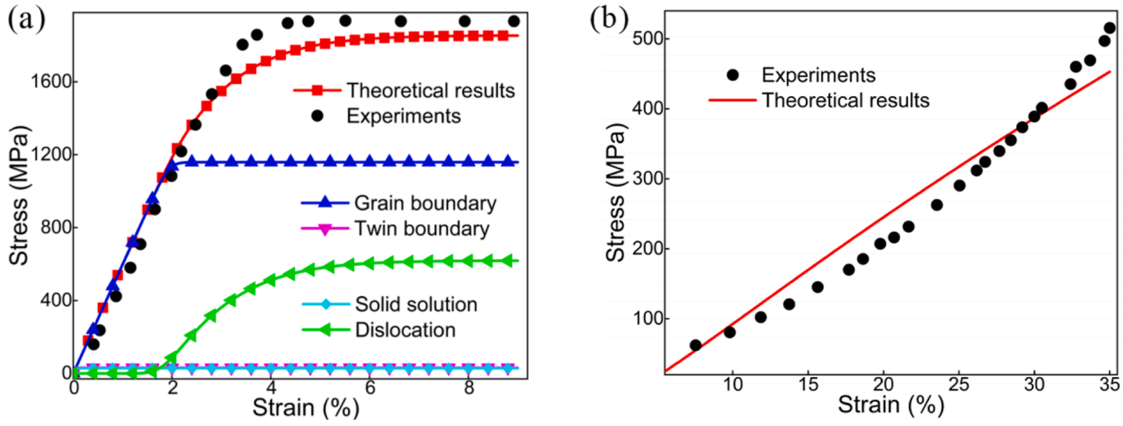

Fig. 17. The stress-strain curve of the $Co_{25}Ni_{25}Fe_{25}Al_{7.5}Cu_{17.5}$ HEA and the individual contributions from the multistage strengthening mechanisms (a). The phase-transformation strengthening of FeCoCrNiMn HEA (b).

Yong Liu: Supervision, Writing - review & editing.
Feng Liu: Conceptualization, Validation, Writing - review & editing, Supervision.
Peter K Liaw: Supervision, Funding acquisition.

Declaration of Competing Interest

The authors declare that they have no known competing financial interests or personal relationships that could have appeared to influence the work reported in this paper.

Data Availability

Data will be made available on request.

Acknowledgements

The authors would like to deeply appreciate the supports from the Foundation for Innovative Research Groups of the National Natural Science Foundation of China (Grant No. 51621004), the National Natural Science Foundation of China (12072109, 51871092, 11772122, and 52020105013), and the State Key Laboratory of Advanced Design and Manufacturing for Vehicle Body (71865015). P. K.L. very much appreciates the support of the National Science Foundation under grants of DMR-1611180 and 1809640 and the US Army Research Office under project numbers of W911NF-13-1-0438 and W911NF-19-2-0049.

References

Afkham, Y., Bahramyan, M., Mousavian, R.T., Brabazon, D., 2017. Tensile properties of AlCrCoFeCuNi glassy alloys: A molecular dynamics simulation study. Mater. Sci. Eng. A 698, 143–151.

Aitken, Z.H., Zhang, Y.W., 2019. Revealing the deformation twinning nucleation mechanism of BCC HEAs. MRS Commun 9 (1), 406–412.

Bahramyan, M., Mousavian, R.T., Brabazon, D., 2020a. Study of the plastic deformation mechanism of TRIP-TWIP high entropy alloys at the atomic level. Int. J. Plast. 127, 102649.

Bahramyan, M., Mousavian, R.T., Brabazon, D., 2020b. Determination of atomic-scale structure and compressive behavior of solidified AlxCrCoFeCuNi high entropy alloys. Int. J. Mech. Sci. 171, 105389.

Cantor, B., Chang, I.T.H., Knight, P., Vincent, A.J.B., 2004. Microstructural development in equiatomic multicomponent alloys. Mater. Sci. Eng. A 375, 213–218.

Chen, B., Li, S., Zong, H., Ding, X., Sun, J., Ma, E., 2020. Unusual activated processes controlling dislocation motion in body-centered-cubic high-entropy alloys. P. Natl. Acad. Sci. 117, 16199–16206.

Chen, T., Lu, W., Li, J., Chen, S., Li, C., Weng, G.J., 2019. Tailoring tensile ductility of thin film by grain size graded substrates. Int. J. Solids. Struct. 166, 124–134.

Chen, G., Qiao, J.W, Jiao, Z.M., Zhao, D., Zhang, T.W., Ma, S.G., Wang, Z.H., 2019. Strength-ductility synergy of Al0.1CoCrFeNi high-entropy alloys with gradient hierarchical structures. Scr. Mater. 167, 95–100.

Chuvil'Deev, V.N., Kopylov, V.I., Nokhrin, A.V., Tryaev, P.V., Kozlova, N.A., Tabachkova, N.Y., Chegurov, M.K., 2017. Study of mechanical properties and corrosive resistance of ultrafine-grained α-titanium alloy Ti-5Al-2V. J. Alloy. Comp. 723, 354–367.

Cowper, G.R., Symonds, P.S., 1957. Strain-hardening and strain-rate effects in the impact loading of cantilever beams. Division of Applied Mathematics.

Cao, F.H., Wang, Y.J., Dai, L.H., 2020. Novel atomic-scale mechanism of incipient plasticity in a chemically complex CrCoNi medium-entropy alloy associated with inhomogeneity in local chemical environment. Acta Mater 194, 283–294.

Daw, M.S., Foiles, S.M., Baskes, M.I., 1993. The embedded-atom method: a review of theory and applications. Mater. Sci. Rep. 9 (7-8), 251–310.

Eleti, R.R., Stepanov, N., Yurchenko, N., Klimenko, D., Zherebtsov, S., 2021. Plastic deformation of solid-solution strengthened Hf-Nb-Ta-Ti-Zr body-centered cubic medium/high-entropy alloys. Scripta Mater 200, 113927.

Eleti, R.R., Stepanov, N., Zherebtsov, S., 2020. Mechanical behavior and thermal activation analysis of HfNbTaTiZr body-centered cubic high-entropy alloy during tensile deformation at 77 K. Scripta Mater 188, 118–123.

Fang, Q., Chen, Y., Li, J., Jiang, C., Liu, B., Liu, Y., Liaw, P.K., 2019. Probing the phase transformation and dislocation evolution in dual-phase high-entropy alloys. Int. J. Plast. 114, 161–173.

Fang, Q., Li, L., Li, J., Wu, H., 2018. Strengthening mechanism of gradient nanostructured body-centred cubic iron film: From inverse Hall-Petch to classic Hall-Petch. Comp. Mater. Sci. 152, 236–242.

Fu, Z., Chen, W., Wen, H., Zhang, D., Chen, Z., Zheng, B., Zhou, Y., Lavernia, E.J., 2016. Microstructure and strengthening mechanisms in an FCC structured single-phase nanocrystalline Co25Ni25Fe25Al7.5Cu17.5 high-entropy alloy. Acta Mater 107, 59–71.

Ganji, R.S., Karthik, P.S., Rao, K.B.S., Rajulapati, K.V., 2017. Strengthening mechanisms in equiatomic ultrafine grained AlCoCrCuFeNi high-entropy alloy studied by micro-and nanoindentation methods. Acta Mater 125, 58–68.

Guo, W., Pei, Z., Sang, X., Poplawsky, J.D., Bruschi, S., Qu, J., Raabe, D., Bei, H., 2019. Shape-preserving machining produces gradient nanolaminate medium entropy alloys with high strain hardening capability. Acta Mater 170, 176–186.

Hahn, G.T., 1962. A model for yielding with special reference to the yield-point phenomena of iron and related bcc metals. Acta Metall 10 (8), 727–738.

Hasan, M.N., Liu, Y.F., An, X.H., Gu, J., Song, M., Cao, Y., Li, Y.S., Zhu, Y.T., Liao, X.Z., 2019. Simultaneously enhancing strength and ductility of a high-entropy alloy via gradient hierarchical microstructures. Int. J. Plast. 123, 178–195.

He, Z.F., Jia, N., Wang, H.W., Liu, Y., Li, D.Y., Shen, Y.F., 2020. The effect of strain rate on mechanical properties and microstructure of a metastable FeMnCoCr high entropy alloy. Mater. Sci. Eng. A 776, 138982.

Huang, H., Wu, Y., He, J., Wang, H., Liu, X., An, K., Lu, Z., 2017. Phase-transformation ductilization of brittle high-entropy alloys via metastability engineering. Adv. Mater. 29, 1701678.

Huang, R., Zhang, Q., Zhang, X., Li, J., Cao, T., Yao, J., Xue, Y., Gao, H., Li, X., 2021. Dynamic recrystallization-induced temperature insensitivity of yield stress in single-crystal Al1.2CrFeCoNi micropillars. Sci. China Technol. Sc. 64 (1), 11–22.

Jian, W.R., Xie, Z., Xu, S., Su, Y., Yao, X., Beyerlein, I.J., 2020. Effects of lattice distortion and chemical short-range order on the mechanisms of deformation in medium entropy alloy CoCrNi. Acta Mater 199, 352–369.

Jin, G., Cai, Z., Guan, Y., Cui, X., Liu, Z., Li, Y., Dong, M., 2018. High temperature wear performance of laser-cladded FeNiCoAlCu high-entropy alloy coating. Appl. Surf. Sci. 445, 113–122.

Kireeva, I.V., Chumlyakov, Y.I., Vyrodova, A.V., Pobedennaya, Z.V., Karaman, I., 2020. Effect of twinning on the orientation dependence of mechanical behaviour and fracture in single crystals of the equiatomic CoCrFeMnNi high-entropy alloy at 77K. Mater. Sci. Eng. A 784, 139315.

Kocks, U.F., Mecking, H., 2003. Physics and phenomenology of strain hardening: the FCC case. Prog. Mater. Sci. 48, 171–273.

Kumar, N., Ying, Q., Nie, X., Mishra, R.S., Tang, Z., Liaw, P.K., Cho, K.C., 2015. High strain-rate compressive deformation behavior of the Al0.1CrFeCoNi high entropy alloy. Mater. Des. 86, 598–602.

Lam, T.N., Lee, S.Y., Tsou, N.T., Chou, H.S., Lai, B.H., Chang, Y.J., Feng, R., Kawasaki, T., Harjo, S., Liaw, P.K., Yeh, A.C., Li, M.J., Cai, R.F., Lo, S.C., Huang, E.W., 2020. Enhancement of fatigue resistance by overload-induced deformation twinning in a CoCrFeMnNi high-entropy alloy. Acta Mater 201, 412–424.

Lee, C., Brechtl, J., Liaw, P.K., 2021. Research on bulk-metallic glasses and high-entropy alloys in Peter K. Liaw's group and with his colleagues. Metall. Mater. Trans. A 52 (6), 2033–2093.

Lee, C., Kim, G., Chou, Y., Musicó, B.L., Gao, M.C., An, K., Song, G., Chou, Y.C., Keppens, V., Chen, W., Liaw, P.K., 2020. Temperature dependence of elastic and plastic deformation behavior of a refractory high-entropy alloy. Sci. Adv. 6 (37), eaaz4748.

Lee, K.S., Bae, B., Kang, J.H., Lim, K.R., Na, Y.S., 2017. Multi-phase refining of an AlCoCrFeNi high entropy alloy by hot compression. Mater. Lett. 198, 81–84.

Li, J., Fang, Q., Liu, B., Liu, Y., 2018. Transformation induced softening and plasticity in high entropy alloys. Acta Mater 147, 35–41.

Li, J., Fang, Q., Liu, B., Liu, Y., Jiang, C., 2017. Twinning-governed plastic deformation in a thin film of body-centred cubic nanocrystalline ternary alloys at low temperature. J. Alloy. Compd. 727, 69–79.

Li, J., Fang, Q., Liu, B., Liu, Y., Liu, Y., 2016. Mechanical behaviors of AlCrFeCuNi high-entropy alloys under uniaxial tension via molecular dynamics simulation. RSC Adv 6 (80), 76409–76419.

Li, J., Chen, H., Fang, Q., Jiang, C., Liu, Y., Liaw, P.K., 2020a. Unraveling the dislocation–precipitate interactions in high-entropy alloys. Int. J. Plast. 133, 102819.

Li, J., Chen, H., He, Q., Fang, Q., Liu, B., Jiang, C., Liaw, P.K., 2020b. Unveiling the atomic-scale origins of high damage tolerance of single-crystal high entropy alloys. Phys. Rev. Mater. 4 (10), 103612.

Li, J., Li, L., Jiang, C., Fang, Q., Liu, F., Liu, Y., Liaw, P.K., 2020c. Probing deformation mechanisms of gradient nanostructured CrCoNi medium entropy alloy. J. Mater. Sci. Technol. 57, 85–91.

Li, J., Chen, H., Li, S., Fang, Q., Liu, Y., Liang, L., Wu, H., Liaw, P.K., 2019. Tuning the mechanical behavior of high-entropy alloys via controlling cooling rates. Mater. Sci. Eng. A 760, 359–365.

Li, L, Fang, Q, Li, J, Liu, B, Liu, Y, Liaw, P.K, 2020b. Lattice-distortion dependent yield strength in high entropy alloys. Mater. Sci. Eng. A 784 (139323).

Li, L., Fang, Q., Li, J., Wu, H., 2019. Origin of strengthening-softening trade-off in gradient nanostructured body-centred cubic alloys. J. Alloy. Compd. 775, 270–280.

Li, J., Fang, Q., Liaw, P.K., 2021. Microstructures and properties of high-entropy materials: modeling, simulation, and experiments. Adv. Eng. Mater. 23, 2001044.

Li, R.X., Liaw, P.K., Zhang, Y., 2017. Synthesis of AlxCoCrFeNi high-entropy alloys by high-gravity combustion from oxides. Mater. Sci. Eng. A 707, 668–673.

Li, J.J., Lu, W., Chen, S., Liu, C., 2020. Revealing extra strengthening and strain hardening in heterogeneous two-phase nanostructures. Int. J. Plast. 126, 102626.

Li, J.J., Soh, A.K., 2012. Modeling of the plastic deformation of nanostructured materials with grain size gradient. Int. J. Plast. 39, 88–102.

Li, L., Chen, H., Fang, Q., Li, J., Liu, F., Liu, Y., Liaw, P.K., 2020a. Effects of temperature and strain rate on plastic deformation mechanisms of nanocrystalline high-entropy alloys. Intermetallics 120, 106741.

Li, L., Fang, Q., Li, J., Liu, B., Liu, Y., Liaw, P.K., 2020b. Lattice-distortion dependent yield strength in high entropy alloys. Mater. Sci. Eng. A 784, 139323.

Li, Z., Wang, H., Guo, Q., Li, Z., Xiong, D.B., Su, Y., Zhang, D., 2018. Regain strain-hardening in high-strength metals by nanofiller incorporation at grain boundaries. Nano Lett 18 (10), 6255–6264.

Li, J.J., Weng, G.J., Chen, S., Wu, X., 2017. On strain hardening mechanism in gradient nanostructures. Int. J. Plast. 88, 89–107.

Lin, Y., Yang, T., Lang, L., Shan, C., Deng, H., Hu, W., Gao, F., 2020. Enhanced radiation tolerance of the Ni-Co-Cr-Fe high-entropy alloy as revealed from primary damage. Acta Mater 196, 133–143.

Ma, S.G., Qiao, J.W., Wang, Z.H., Yang, H.J., Zhang, Y., 2015. Microstructural features and tensile behaviors of the Al0.5CrCuFeNi2 high-entropy alloys by cold rolling and subsequent annealing. Mater. Des. 88, 1057–1062.

Maresca, F., Curtin, W.A., 2020. Mechanistic origin of high strength in refractory BCC high entropy alloys up to 1900K. Acta Mater 182, 235–249.

Nguyen, N.T.C., Asghari-Rad, P., Sathiyamoorthi, P., Zargaran, A., Lee, C.S., Kim, H.S., 2020. Ultrahigh high-strain-rate superplasticity in a nanostructured high-entropy alloy. Nat. Commun. 11 (1), 1–7.

Ojha, A., Sehitoglu, H., Patriarca, L., Maier, H.J., 2014. Twin nucleation in Fe-based bcc alloys—modeling and experiments. Model. Simul. Mater. Sci. Eng. 22 (7), 075010.

Park, J.M., Moon, J., Bae, J.W., Jang, M.J., Park, J., Lee, S., Kim, H.S., 2018. Strain rate effects of dynamic compressive deformation on mechanical properties and microstructure of CoCrFeMnNi high-entropy alloy. Mater. Sci. Eng. A 719, 155–163.

Peng, J., Li, F., Liu, B., Liu, Y., Fang, Q.H., Li, J., Liaw, P.K., 2021. Mechanical properties and deformation behavior of a refractory multiprincipal element alloy under cycle loading. J. Micromech. Mol. Phys., 2050014

Plimpton, S., 1995. Fast parallel algorithms for short-range molecular dynamics. J. Comp. Phys. 117, 1–19.

Rida, A., Micoulaut, M., Rouhaud, E., Makke, A., 2020. Understanding the strain rate sensitivity of nanocrystalline copper using molecular dynamics simulations. Comp. Mater. Sci. 172, 109294.

Rao, S.I., Varvenne, C., Woodward, C., Parthasarathy, T.A., Miracle, D., Senkov, O.N., Curtin, W.A., 2017. Atomistic simulations of dislocations in a model BCC multicomponent concentrated solid solution alloy. Acta Mater 125, 311–320.

Sathiyamoorthi, P., Kim, H.S., 2020. High-entropy alloys with heterogeneous microstructure: processing and mechanical properties. Prog. Mater. Sci., 100709

Shi, P., Zhong, Y., Li, Y., Ren, W., Zheng, T., Shen, Z., Yang, B., Peng, J.C., Hu, P.F., Zhang, Y., Liaw, P.K., Zhu, Y.T., 2020. Multistage work hardening assisted by multi-type twinning in ultrafine-grained heterostructural eutectic high-entropy alloys. Mater. Tod. 41, 62–71.

Shuang, S., Ding, Z.Y., Chung, D., Shi, S.Q., Yang, Y., 2020. Corrosion resistant nanostructured eutectic high entropy alloy. Corros. Sci. 164, 108315.

Sriharitha, R., Murty, B.S., Kottada, R.S., 2014. Alloying, thermal stability and strengthening in spark plasma sintered AlxCoCrCuFeNi high entropy alloys. J. Alloy. Compd. 583, 419–426.

Stukowski, A., 2009. Visualization and analysis of atomistic simulation data with OVITO-the Open Visualization Tool. Model. Simul. Mater. Sci. Eng. 18, 015012.

Sun, Y., Chen, P., Liu, L., Yan, M., Wu, X., Yu, C., Liu, Z., 2018. Local mechanical properties of AlxCoCrCuFeNi high entropy alloy characterized using nanoindentation. Intermetallics 93, 85–88.

Tsianikas, S., Chen, Y., Jeong, J., Zhang, S., Xie, Z., 2021. Self-toughened high entropy alloy with a body-centred cubic structure. Nanoscale 13, 3602–3612.

Wang, J., Zeng, Z., Weinberger, C.R., Zhang, Z., Zhu, T., Mao, S.X., 2015. In situ atomic-scale observation of twinning-dominated deformation in nanoscale body-centred cubic tungsten. Nat. Mater. 14 (6), 594–600.

Wang, F., Balbus, G.H., Xu, S., Su, Y., Shin, J., Rottmann, P.F., Knipling, K.E., Stinville, J.C., Mills, L.H., Senkov, O.N., Beyerlein, I.J., Pollock, T.M., Gianola, D.S., 2020. Multiplicity of dislocation pathways in a refractory multiprincipal element alloy. Science 370, 95–101.

Wang, Z., Lin, X., Kang, N., Hu, Y., Chen, J., Huang, W., 2020. Strength-ductility synergy of selective laser melted Al-Mg-Sc-Zr alloy with a heterogeneous grain structure. Addit. Manuf. 34, 101260.

Wang, Z., Wang, C., Zhao, Y.L., Hsu, Y.C., Li, C.L., Kai, J.J., Liu, C.T., Hsueh, C.H., 2020. High hardness and fatigue resistance of CoCrFeMnNi high entropy alloy films with ultrahigh-density nanotwins. Int. J. Plast. 131, 102726.

Wang, P., Bu, Y., Liu, J., Li, Q., Wang, H., Yang, W., 2020. Atomic deformation mechanism and interface toughening in metastable high entropy alloy. Mater. Tod. 37, 64–73.

Wang, S., Wu, M., Shu, D., Zhu, G., Wang, D., Sun, B., 2020. Mechanical instability and tensile properties of TiZrHfNbTa high entropy alloy at cryogenic temperatures. Acta Mater 201, 517–527.

Wei, Y., 2011. Scaling of maximum strength with grain size in nanotwinned fcc metals. Phys. Rev. B 83 (13), 132104.

Wu, X., Zhu, Y., Lu, K., 2020. Ductility and strain hardening in gradient and lamellar structured materials. Scripta Mater 186, 321–325.

Xu, S., Su, Y., Jian, W.R., Beyerlein, I.J., 2021. Local slip resistances in equal-molar MoNbTi multi-principal element alloy. Acta Mater 202, 68–79.

Xu, X.D., Liu, P., Tang, Z., Hirata, A., Song, S.X., Nieh, T.G., Liaw, P.K., Liu, C.T., Chen, M.W., 2018. Transmission electron microscopy characterization of dislocation structure in a face-centered cubic high-entropy alloy Al0.1CoCrFeNi. Acta Mater 144, 107–115.

Yang, M., Yan, D., Yuan, F., Jiang, P., Ma, E., Wu, X., 2018. Dynamically reinforced heterogeneous grain structure prolongs ductility in a medium-entropy alloy with gigapascal yield strength. P. Nati. Acad. Sci. 115 (28), 7224–7229.

Yeh, J.W., Chen, S.K., Lin, S.J., Gan, J.Y., Chin, T.S., Shun, T.T., Tsau, C.H., Chang, S.Y., 2004. Nanostructured high-entropy alloys with multiple principal elements: novel alloy design concepts and outcomes. Adv. Eng. Mater. 6 (5), 299–303.

Zepeda-Ruiz, L.A, Stukowski, A, Oppelstrup, T., Bulatov., V.V., 2017. Probing the limits of metal plasticity with molecular dynamics simulations. Nature 550, 492.

Zhang, C., Zhu, C., Cao, P., Wang, X., Ye, F., Kaufmann, K., Casalena, L., MacDonalda, B.E., Pan, X., Vecchio, K., Lavernia, E.J., 2020. Aged metastable high-entropy alloys with heterogeneous lamella structure for superior strength-ductility synergy. Acta Mater 199, 602–612.

Zhang, T.W., Jiao, Z.M., Wang, Z.H., Qiao, J.W., 2017. Dynamic deformation behaviors and constitutive relations of an AlCoCr1. 5Fe1. 5NiTi0. 5 high-entropy alloy. Scripta Mater 136, 15–19.

Zhang, T., Zhao, R.D., Wu, F.F., Lin, S.B., Jiang, S.S., Huang, Y.J., Eckert, J., 2020. Transformation-enhanced strength and ductility in a FeCoCrNiMn dual phase high-entropy alloy. Mater. Sci. Eng. A 780, 139182.

Zhang, Y., Millett, P.C., Tonks, M., Biner, B., 2012. Deformation-twin-induced grain boundary failure. Scripta Mater 66 (2), 117–120.

Zhao, L., Zong, H., Ding, X., Lookman, T., 2021. Anomalous dislocation core structure in shock compressed bcc high-entropy alloys. Acta Mater 209, 116801.

Zhu, L., Ruan, H., Li, X., Dao, M., Gao, H., Lu, J., 2011. Modeling grain size dependent optimal twin spacing for achieving ultimate high strength and related high ductility in nanotwinned metals. Acta Mater 59 (14), 5544–5557.

Zhu, Y.T, Ameyama, K., Anderson, P.M., Beyerlein, I.J., Gao, H., Kim, H.S., Zhang, X., Wu, X., 2021. Heterostructured materials: superior properties from hetero-zone interaction. Mater. Res. Lett. 9 (1), 1–31.

Zhu, Y.T., Liao, X.Z., Wu, X.L., 2012. Deformation twinning in nanocrystalline materials. Prog. Mater. Sci. 57 (1), 1–62.

Zhou, X.W., Johnson, R.A., Wadley, H.N.G., 2004. Misfit-energy-increasing dislocations in vapor-deposited CoFe/NiFe multilayers. Phys. Rev. B 69, 144113.